

Building the confined CoS₂/MoS₂ nanoreactor via interface electronic reconfiguration to synchronously enhance activity and stability of heterogeneous Fenton-like reactions

Zhimo Fang ^a, Yuangu Xia ^a, Lin Zhang ^b, Ji Liu ^a, Jihong Li ^a, Bin Hu ^a, Kai Li ^a, Qiang Lu ^{a,*}, Lidong Wang ^{b,*}

^a National Engineering Research center of New Energy Power Generation, North China Electric Power University, Beijing 102206, China

^b College of Environmental Science and Engineering, North China Electric Power University, Beijing 102206, China



ARTICLE INFO

Keywords:
Interface
Confined nanoreactor
CoS₂/MoS₂ catalysts
SO₄²⁻ radicals
Fenton-like reactions

ABSTRACT

Herein, we synthesized CoS₂/MoS₂ catalysts with vertical interface structures to enhance peroxyomonosulfate (PMS) activation. The characterization, experimental, and calculation results jointly reveal that the strong interface interaction (Co–S–Mo bond) regulates the electronic structure of CoS₂/MoS₂ to optimize the generation process of the main reactive oxygen species (SO₄²⁻) and stabilizes the coordination structure of the active sites to greatly improve catalytic robustness. The unique interface structure of CoS₂/MoS₂ constructs the confined nanoreactor to adsorb pollutants and capture pollutant electrons, which can shorten the migration distance of SO₄²⁻ and improve the electron transfer rate, ultimately increasing the utilization and conversion rate of PMS. CoS₂/MoS₂ achieved outstanding activity (0.302 min⁻¹), stability (93% of reactivity maintained after eight runs), and acid-base resistance (working pH range 3–11) for sulfamethazine degradation. This work provides a clear perspective for the rational design and optimization of interface engineering-mediated dual component catalysts in the Fenton-like reactions.

1. Introduction

Medical sewage containing a large number of chemical agents and pathogenic microorganisms, without undergoing harmless treatment such as disinfection and inactivation, is directly discharged into urban sewers, often causing water and soil pollution, and in severe cases, leading to the outbreak of water-borne infectious diseases [1–4]. Fenton-like reactions based on peroxyomonosulfate (PMS) stand out among water treatment technologies because of their compelling advantages, such as rapid oxidation, high mineralization, and ease of transport and storage [5–7]. PMS can readily decompose into reactive oxygen species (ROS) with the short lifespans, such as hydroxyl radicals (•OH), sulfate radicals (SO₄²⁻), and singlet oxygen (¹O₂), through electron-transferring processes [8–10]. The tardy kinetics of PMS in the above process leads to prohibitive costs and substantial chemical inputs. In order to improve the activation level of PMS, many studies have extended homogeneous reaction systems to heterogeneous reaction systems. The ideal catalyst must work efficiently and stably over a wide range of pH condition, thus making the PMS activation process more reliable [11,12].

The half-metallic pyrite-type CoS₂ has been extensively applied in energy conversion and storage applications due to the earth's abundant, modifiable electronic structure of Co and the high synergy between Co and S species [13]. CoS₂, a novel cubic crystal structure, only possesses Co octahedral site (coordinated to the 6 S atoms) with the 3d⁷ electronic structure [14]. 3d orbital can be split to t_{2g}⁶e_g¹ due to the strong crystal field, which would endow the catalyst with excellent electron transfer ability, but meanwhile may result in a loosening of the coordination structure to affect the catalyst stability [15]. The interfacial effect in the catalyst is the interaction between different components, which brings emerging possibilities to improve the activity and stability of the catalysts [16]. Studies have proved that interface engineering exhibits extraordinary advantages in optimizing the interfacial electronic structure, regulating the catalyst surface adsorption/desorption processes, inhibiting severe agglomeration of catalysts, and preventing the shedding of active site [17–19]. Meanwhile, bimetallic components have been demonstrated to enhance the PMS activation performance of catalysts [20,21]. Therefore, we deduce that the rational design of bimetallic sulfide via interface engineering can maximize the catalyst function.

* Corresponding authors.

E-mail addresses: qianglu@mail.ustc.edu.cn, qlu@ncepu.edu.cn (Q. Lu), wld@ncepu.edu.cn (L. Wang).

The salient anisotropic properties and structural flexibility make MoS₂ versatile for various catalytic reactions [22,23]. Yan et al. reported a pioneering work on using MoS₂ as a co-catalyst in Fenton-like reactions [24,25]. Combining CoS₂ and MoS₂ into reasonably ordered heterostructures can achieve rapid charge transfer between Mo and Co through S atoms as a bridge to enhance catalytic activity [18,25]. Meanwhile, the difference in work function between dual components leads to the rearrangement of electrons at the interface, which may reconstruct active sites' electronic structure and density to sweeten the stability of the Co-S bond in CoS₂. Li et al. reported that MoS₂ could adsorb organics through the combined effects of multiple affinities such as π - π interaction, hydrophobic effect, surface complexation, and hydrogen bond [26]. MoS₂ can enrich some electron-rich organic molecules on the catalyst surface to achieve nanoscale spatial limitation, which can significantly shorten the migration distance of ROS to pollutants to improve the inherent defect of ROS in the Fenton-like reaction [27]. Therefore, it is necessary to determine the role of the different components in controlling the catalytic behavior to achieve the targeted design of multifunctional catalysts.

Based on the above inspiration, we synthesized CoS₂/MoS₂ catalysts with a vertical interfacial structure for the PMS activation. The characterizations and calculations were combined to indicate that the charge recombination via the strong interfacial interaction (Co—S—Mo bond) formed at the interface between MoS₂ and CoS₂ could not only improve the stability of the coordination structure, but also provide the interface Co with abundant zero-filling e_g orbitals as new PMS adsorption sites to reduce the energy barrier of PMS activation for enhanced the main ROS generation (SO₄^{•-}). The confined nanoreactor was established to absorb sulfamethazine (SMT, target pollutant) and capture SMT electrons through the exposed edge S sites of the vertical interface structure in CoS₂/MoS₂, which could shorten the mass transfer distance of short-life SO₄^{•-} radicals and transport captured electrons to improve the utilization and conversion rate of PMS. The experimental results declared that CoS₂/MoS₂ catalyst exhibited a rapid SMT removal efficiency (100% within 10 min), long-term stability, and excellent acid-base resistance (working pH range 3–11). Our findings revealed the intrinsic origin of the superior activity of CoS₂/MoS₂ for PMS activation, which would inspire the application of the interface engineering strategy in Fenton-like reactions.

2. Experimental section

2.1. Catalyst synthesis

All the chemicals and reagents were detailed in Text S1, Supporting Information (SI). Deionized/pure water samples in the experiment were all prepared by the laboratory pure water mechanism. Firstly, ZIF-67 was prepared by a typical autonomous assembly method, which was detailed in Text S2. Secondly, CoS₂ was prepared by the solvothermal method using ZIF-67 as the template: 120 mg ZIF-67 was ultrasonic dispersed in 60 mL ethanol, and then 240 mg thioacetamide (TAA) was added. After stirring for 30 min, the mixture was transferred into a 100 mL Teflon lined autoclave at 160 °C for 6 h. The solid was collected by centrifugation, washed with deionized water and ethanol for three times, and dried under vacuum at 60 °C for 12 h to obtain a black solid powder of CoS₂. Finally, MoS₂ was coated on the outside of CoS₂ by hydrothermal method to form CoS₂/MoS₂ composites: 20 mg CoS₂ was ultrasonically dispersed in 60 mL deionized water, then 60 mg/120 mg/240 mg Na₂MoO₄·2 H₂O was added for 2 h stirring, and 40 mg/80 mg/120 mg TAA was added to stir to completely dissolve, and the mixture was transferred into a 100 mL Teflon lined autoclave at 210 °C for 20 h. After cooling to room temperature, the solid was collected by centrifugation, washed with deionized water and ethanol three times, and dried under vacuum at 60 °C for 12 h to obtain black solid powders of CoS₂/MoS₂-x (x = 1, 2 and 3), which were generally referred to CoS₂/MoS₂-2 without special instructions. Roughly calculated based on the complete

conversion of Mo in Na₂MoO₄·2 H₂O into MoS₂, the mass ratio of CoS₂ to MoS₂ is 1:2, 1:4, and 1:8 in CoS₂/MoS₂-x (x = 1, 2 and 3), respectively. Generally, CoS₂/MoS₂ referred to CoS₂/MoS₂-2 without special explanation. Likely, the individual MoS₂ was prepared under identical conditions in the absence of CoS₂, which was detailed in Text S2. Mix CoS₂ and MoS₂ with a mass ratio of 1:4 by grinding for 5 min to prepare CoS₂ + MoS₂.

2.2. Catalytic experiment

Fenton-like reaction occurred in a 150 mL beaker by first adding 100 mL solution containing 10 mg/L SMT and then adding 400 μ L PMS solution (0.1 M) with magnetic stirring. Experiments were triggered by the addition of 15 mg catalyst, and then 1.5 mL sample and 100 μ L Na₂S₂O₃ (100 mM, reaction terminator) were passed over 0.22 μ M nylon filtration membrane filtered into sample vials. The concentration of SMT and other organic compound was analyzed by high-performance liquid chromatography (HPLC, Wayyeal LC3200) with C18 chromatographic column, which was detailed in Table S1. The diluted sulfuric acid and sodium hydroxide solutions were used to adjust the initial pH. Intermediates of SMT were detected by HPLC-MS. The evaluation methods of SMT decomposition ratio and the rate constant (k_1) calculation process were provided.

The methods to evaluate and determine the removal efficiency of SMT in different processes were as follows:

$$\text{Removal efficiency (\%)} = 100 \times (C_0 - C) / C_0 \quad (1)$$

where C_0 and C (mg L⁻¹) represent the initial concentration and instant concentration at areaction time of SMT, respectively.

The pseudo-first-order kinetics model:

$$\ln(C/C_0) = -k_1 t \quad (2)$$

where C_0 , C and k_1 represent the initial concentration, instant concentration at reaction time, and rate constant, respectively.

2.3. Methodology

This subsection including catalyst characterization methods, quantitative analysis of PMS, quantitative analyses of •OH, SO₄^{•-}, and ¹O₂, calculation method for ROS contribution rate, and density functional theory (DFT) calculation methods were detailed in Texts S3-S7.

3. Results and discussion

3.1. Fabrication and characterization of catalysts

The preparation process of the CoS₂/MoS₂ catalyst was described in Fig. 1a. Briefly, CoS₂ was synthesized using cobalt-based zeolitic imidazolate frameworks (ZIF-67) as the template through the Kirkendall effect, and MoS₂ nanosheets could be grown vertically on CoS₂ by in situ hydrothermal methods to form CoS₂/MoS₂ with the Co—S—Mo bond. In order to intuitively prove the successful synthesis of composite materials, scanning electron microscopy (SEM) and transmission electron microscopy (TEM) characterization were carried out. CoS₂ was a hollow dodecahedron with a diameter of about 600 nm (Fig. 1b and c) and MoS₂ was stacked with individual nanosheets (Fig. 1d and e). MoS₂ nanosheets covered the hollow CoS₂ uniformly and vertically and revealed the formation of heterojunctions between CoS₂ and MoS₂ (Fig. 1f and g). High-resolution TEM (HRTEM) results declared a close anchoring-retention interface in the CoS₂/MoS₂ heterostructure, and the lattice stripe spacings of 0.24 and 0.63 nm belonged to CoS₂ (210) and MoS₂ (002) (Fig. 1h) [28], respectively. Meanwhile, the energy-dispersive spectroscopy (EDS) elemental mappings indicated Co, Mo, and S elements corresponded to the CoS₂/MoS₂ having a uniform distribution, and it is obvious to see that the ultrathin MoS₂ nanosheets covered with

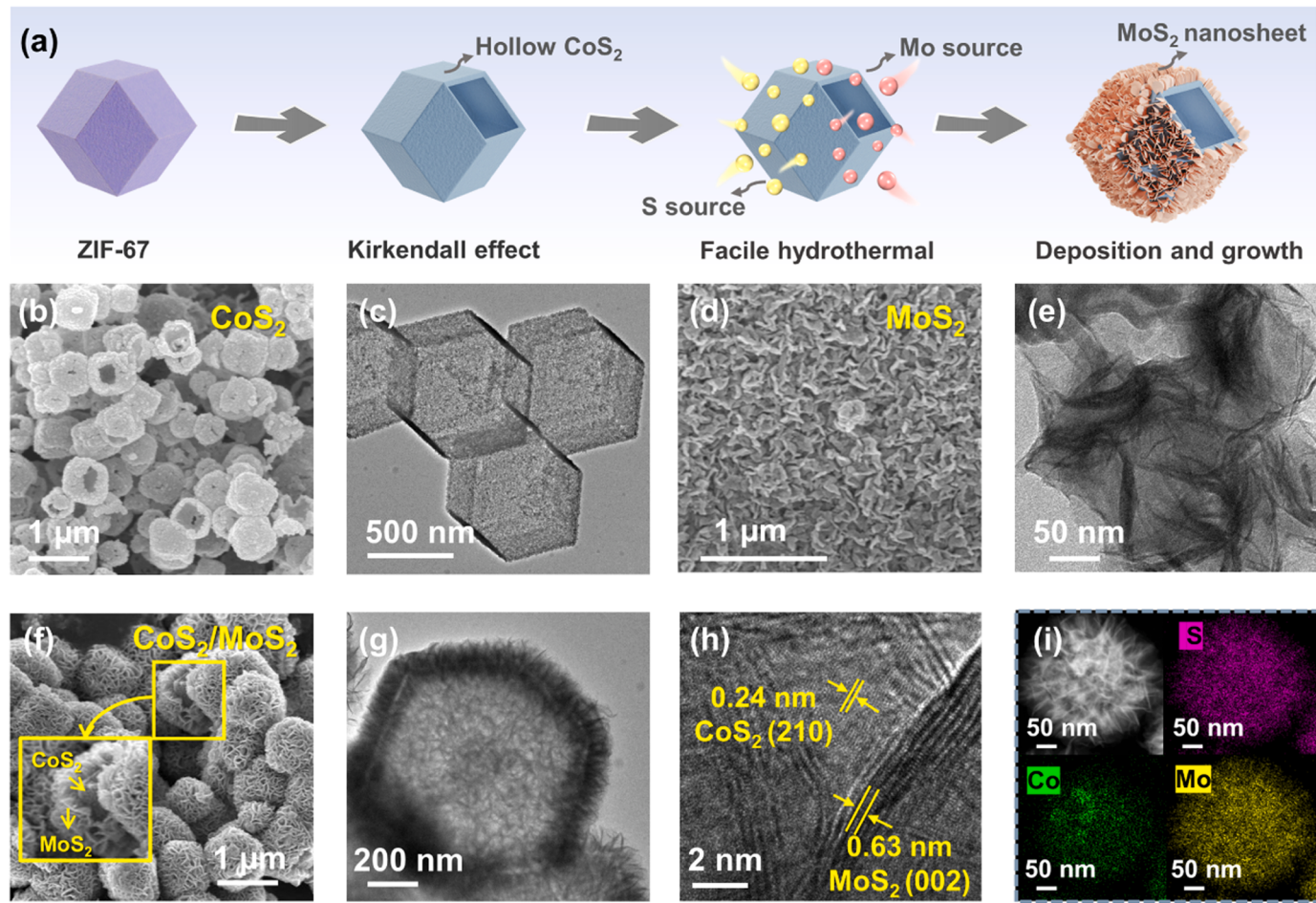


Fig. 1. (a) The synthetic scheme. (b) SEM and (c) TEM images of CoS₂. (d) SEM and (e) TEM images of MoS₂. (f) SEM, (g) TEM (h) HRTEM, and (i) EDS-mapping of CoS₂/MoS₂.

hollow CoS₂ were observed, which further confirmed the successful synthesis of CoS₂/MoS₂ core-shell structure (Fig. 1i) [25].

The crystal phase compositions were further studied by X-ray diffraction (XRD) analysis. The three samples matched well with the CoS₂ and MoS₂ standard card (PDF #41–1471 and 75–1539), consistent with the HRTEM results (Fig. 2a). Raman spectra further demonstrated the vertical edge-oriented structure of MoS₂ (Fig. 2b). Typical in-plane E_g (280.2 cm⁻¹) and out-of-plane A_{1g}⁽¹⁾ (390.5 cm⁻¹) phonon modes of Co–S were shown in the individual CoS₂ [29]. Meanwhile, the peaks at 404.8 and 382.5 cm⁻¹ corresponded to out-of-plane vibration (A_{1g}) and in-plane vibration (E_{2g}) of Mo–S of 2 H phase MoS₂ [30]. Notice that the Raman peak corresponding to the out-of-plane Mo–S phonon mode (A_{1g}) was preferentially excited for the edge-terminated film due to the polarization dependence, whereas the in-plane Mo–S phonon mode (E_{2g}) was preferentially excited for the terrace-terminated film [31], as illustrated in the inset of Fig. 2b. Since the intensity ratio of A_{1g}/E_{2g} in CoS₂/MoS₂ was significantly higher than that in MoS₂, the vertical superposition of MoS₂ formed on CoS₂ could expose more edges S [32], which was consistent with the HRTEM results. In addition, the two peaks of A_{1g} and E_{2g} belonging to MoS₂ in CoS₂/MoS₂ had a slight blue shift compared with pure MoS₂, and A_{1g}⁽¹⁾ and E_g belonging to CoS₂ in CoS₂/MoS₂ had a slight red shift compared with pure CoS₂, indicating that there was a close covalent interaction via Co–S–Mo bond between CoS₂ and MoS₂ in the CoS₂/MoS₂ [25].

X-ray photoelectron spectroscopy (XPS) spectrum detected the chemical state of Co, Mo, and S elements, providing evidence for the coupling between CoS₂ and MoS₂ (Fig. 2c and d). More detailed analysis would be provided in Text S8. The peaks shift proved that electrons were

transferred from CoS₂ to MoS₂ [18]. The signal at 164.8 eV confirmed the presence of bridged disulfide S₂²⁻ and/or apical S₂²⁻ ligands, which were significantly increased in CoS₂/MoS₂ compared with MoS₂, indicating enhanced S-edge site exposure [33]. All the results confirmed the formation of the vertical CoS₂/MoS₂ heterostructure. Such a vertical stacking manner might be beneficial for molecular directed mass transfer and edge site exposure for catalytic promotions [25]. In order to understand the formation of the internal electric field and the mechanism of charge transfer at the interface, the first-principles calculation was carried out using DFT. The work functions were obtained from the surface electrostatic potential of the material (Fig. 2e), which was an essential physical parameter to determine the band orientation and free electron transfer at the interface [34,35]. The result declared that the work function of MoS₂ (5.77 eV) was higher than CoS₂ (4.88 eV), indicating that the electrons would flow from CoS₂ to MoS₂ at the dense interface [36]. In addition, the planar-averaged electron density difference ($\Delta\rho$) and three-dimensional charge density difference could be used to verify this result visually (Fig. 2f). The green and red regions on the built CoS₂/MoS₂ model in inset of Fig. 2f represented the electron depletion and aggregation regions, respectively. Notice that charge redistribution occurred near the interface of the CoS₂/MoS₂ composite, and electrons accumulated on the MoS₂ side of the interface [37]. DFT results revealed that the CoS₂ part was positively charged near the interface, while the MoS₂ part was negatively charged due to electron migration, which was verified with XPS results.

The atomic local structure of the CoS₂/MoS₂ was further confirmed by X-ray absorption fine structure (XAFS) measurement, an elemental sensitive technique. In Fig. 3a, the normalized X-ray absorption near-

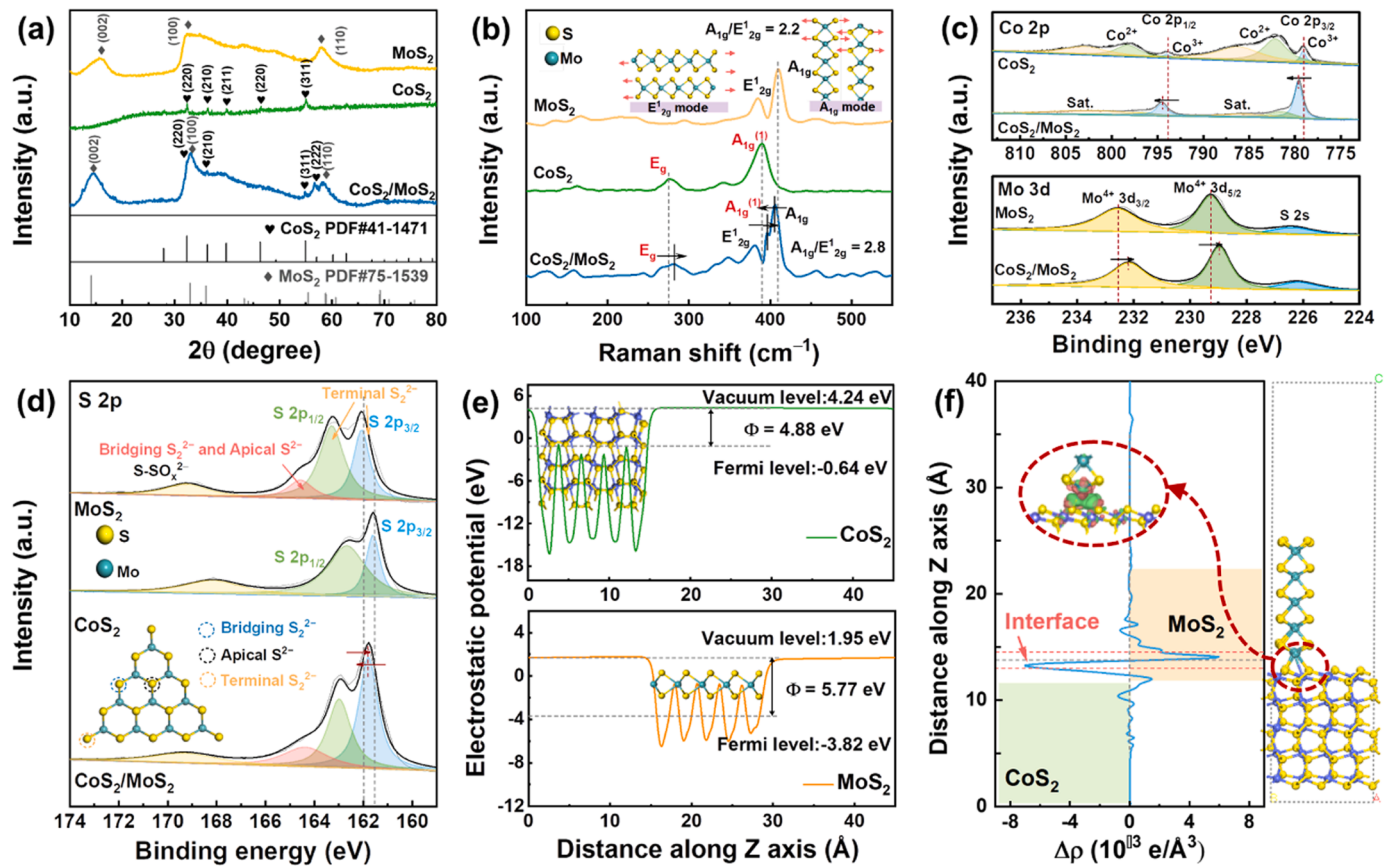


Fig. 2. (a) XRD patterns, (b) Raman spectra, (c-d) Co 2p, Mo 3d, and S 2p of as-prepared catalysts. (e) CoS₂ and MoS₂ of the calculated work function and the corresponding structural models. (f) CoS₂/MoS₂ of planar-averaged electron density difference and the corresponding structural model (inset: side view of the charge density difference over the CoS₂/MoS₂).

edge structure (XANES) curves of Co K-edge revealed that the absorption edge of the CoS₂/MoS₂ was higher-energy shifted than that of CoS₂, suggesting that the average oxidation state of Co in the CoS₂/MoS₂ was more positive, mainly due to the modulation of the interface charge. The Fourier transform (FT) extended X-ray absorption fine structure (EXAFS) (Fig. 3b) of the CoS₂/MoS₂ possessed only one main peak located at 1.58 Å, which was assigned to Co–S coordination. The distance was shorter than that of CoS₂ (1.65 Å), revealing the possible shrinking of Co–S bonds. Quantitative EXAFS analysis was also performed. The EXAFS fitting curves of the CoS₂/MoS₂ were displayed in Fig. 3c and f. XANES curves of Mo K-edge in Fig. 3d indicated that the average valence state of Mo in the CoS₂/MoS₂ sample was between 0 and +4, further confirming the XPS and DFT results. The Mo K-edge EXAFS of the CoS₂/MoS₂ in Fig. 3e showed two peaks (1.92 and 2.95 Å) which belonged to the Mo–S and Mo–Mo coordination. The decreased intensity of peaks in CoS₂/MoS₂ compared with MoS₂ indicated that Mo atoms in MoS₂ was connected with CoS₂ via Co–S–Mo covalent bond [23]. The local structural parameters of the CoS₂/MoS₂ were listed in Table S2. The EXAFS fitting results indicated that the averaged length of Co–S bond was 2.20 Å and Mo–S bond was 2.39 Å, which were smaller than those of CoS₂ reference (2.31 Å) and MoS₂ reference (2.41 Å). DFT further validated the above results (Fig. S1), indicating that the model was constructed reasonably and that the formation of the interface between CoS₂ and MoS₂ resulted in changes in valence states and bond lengths. In summary, the special interface structure could not only enhance the exposure of MoS₂ edges, but also enhance stability by tightly connecting CoS₂ and MoS₂ through covalent bonds of Co–S–Mo type instead of common van der Waals connection.

3.2. Evaluation of Fenton-like catalytic activity

The catalytic activity of the as-synthesized catalysts was first estimated through SMT adsorption efficiency, SMT removal efficiency, SMT degradation kinetics, and total organic carbon (TOC) removal efficiency (Fig. 4a-c). The composites synthesized with different mass ratios were marked as CoS₂/MoS₂-1, CoS₂/MoS₂-2, and CoS₂/MoS₂-3. The adsorption experiments demonstrated that CoS₂ alone possessed almost no SMT adsorption capacity. CoS₂/MoS₂-3 reached the highest SMT adsorption efficiency (26.7%), which might be attributed to the increase in the specific surface area of the catalysts (Fig. S2) [26]. For SMT degradation process, the SMT removal rate was significantly higher than that by the adsorption system or using PMS alone (named “blank”), confirming the superiority of the PMS activation process. It could be observed that the inability of MoS₂ alone to active PMS, which might be attributed to the fact that 2 H phase MoS₂ was not the active phase for PMS activation and the weak activation effect of MoS₂ on PMS is difficult to generate a large amount of ROS for SMT degradation [38]. SMT removal might be attributed to the adsorption effect in the MoS₂/PMS system. Meanwhile CoS₂ alone could remove 78.6% of SMT (rate constant $\sim 0.162 \text{ min}^{-1}$) which might be due to Co²⁺ being an excellent active metal for PMS [39]. Excluding CoS₂ without adsorption capacity, the degradation rate constant was found to be related to the extent of SMT adsorption by the catalysts. CoS₂/MoS₂-2 reached the superior degradation kinetics (rate constant $\sim 0.302 \text{ min}^{-1}$) and degree of mineralization (71.6% TOC removal within 2 h) among as-synthesized catalysts. The degradation ability of CoS₂/MoS₂-3 was lower than that of CoS₂/MoS₂-2, possibly due to the excessive amount of MoS₂ wrapped on the CoS₂, which could not expose the PMS activation site. CoS₂/MoS₂-2 was selected for further study named CoS₂/MoS₂. It was

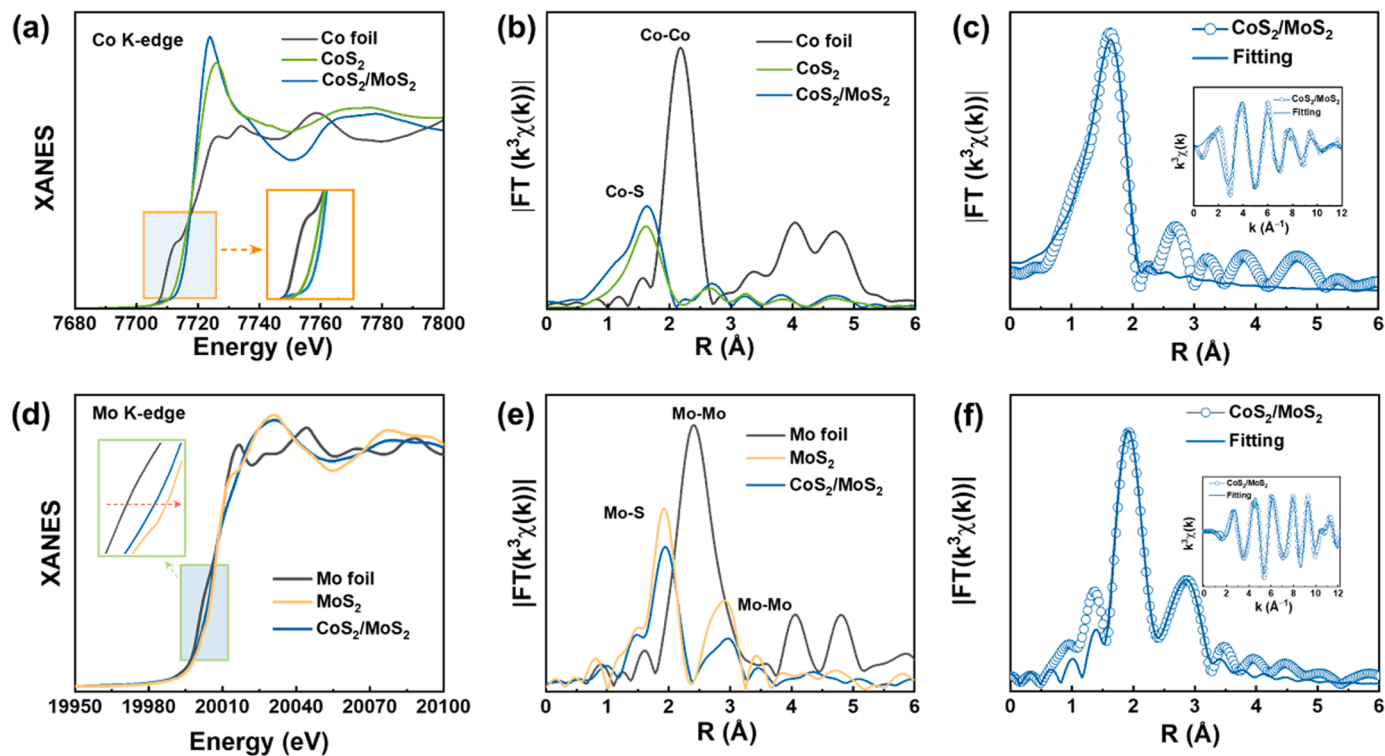


Fig. 3. (a) Normalized Co K-edge XANES and (b) Fourier transform of Co K-edge EXAFS spectra of $\text{CoS}_2/\text{MoS}_2$ and reference samples. (c) The Co K-edge EXAFS fitting curves of the $\text{CoS}_2/\text{MoS}_2$. (d) Normalized Mo K-edge XANES and (e) Fourier transform of Mo K-edge EXAFS spectra of $\text{CoS}_2/\text{MoS}_2$ and reference samples. (f) The Mo K-edge EXAFS fitting curves of the $\text{CoS}_2/\text{MoS}_2$.

noteworthy that $\text{CoS}_2/\text{MoS}_2$ also had higher activity than physically mixed ($\text{CoS}_2 + \text{MoS}_2$), suggesting a strong interaction between the CoS_2 and MoS_2 components in the $\text{CoS}_2/\text{MoS}_2$. The enrichment of reactants was considered a key manifestation of the nano confinement effect in the nanoreactor microenvironment. When the active site was loaded internally, an increase in local reactant concentration would result in a higher reaction rate. Fig. 4d indicated that the increase in catalyst concentration led to an increase in the concentration of SMT enrichment in the nanoreactor. The enrichment degree (adsorption efficiency) of SMT was positively correlated with its degradation performance, which was consistent with the reported results of the confined Fenton-like reaction [40,41]. The enrichment of reactants was considered a key manifestation of the confinement effect in the microenvironment of nanoreactors. $\text{CoS}_2/\text{MoS}_2$ with a vertical interface structure exhibited superior PMS activation ability compared to individual CoS_2 (Fig. 4e). Meanwhile, the addition of SMT only increased the PMS consumption in the $\text{CoS}_2/\text{MoS}_2/\text{PMS}$ system, indicating that $\text{CoS}_2/\text{MoS}_2$ adsorbed SMT on the edge S of MoS_2 and might capture SMT electrons to further accelerate PMS activation. The degradation rate gradually increased as the concentration of PMS increased (Fig. 4f), indicating that the $\text{CoS}_2/\text{MoS}_2$ catalyst had excellent ability of PMS activation. The degradation rate decreased when the SMT concentration changed from 5 mg/L to 20 mg/L (Fig. 4g), which might be attributed to the limitation of the number of adsorption sites and the relatively small number of ROSs relative to pollutants.

Different influencing factors were explored to evaluate the degradation anti-interference of the $\text{CoS}_2/\text{MoS}_2/\text{PMS}$ system. The effect of the different initial pH values (3.0–11.0) on SMT degradation was studied to reveal the specificity of the $\text{CoS}_2/\text{MoS}_2/\text{PMS}$ system for initial pH values (Figs. 4h and S3a). $\text{CoS}_2/\text{MoS}_2$ could retain excellent activities in all initial pH values, which might be attributed to the protective performance of the vertical interface structure [42]. Under the initial pH of 7, the dynamic changes in pH during the degradation of SMT were monitored. Fig. S3b indicated that the pH value decreased from the initial 7.0

to 5.9, which might be attributed to the catalytic decomposition of PMS, the formation of acidic intermediates, the buffering effect of the catalyst, and the oxidation of water molecules by sulfate ions generated by PMS activation [43,44]. The reaction rate constant was slightly promoted in the presence of Cl^- (Figs. 4h and S3c), which might be attributed to the fact that Cl^- could react with $\text{HSO}_5^-/\text{SO}_4^{2-}/\cdot\text{OH}$ to produce reactive chlorine species (HClO , $\text{Cl}\bullet$, $\text{Cl}_2\bullet^-$, and $\text{ClO}\bullet$) with strong oxidation ability [45]. In addition, the PMS activation performance of the $\text{CoS}_2/\text{MoS}_2$ was almost unaffected by the common anions (CO_3^{2-} and HPO_4^{2-}), indicating that $\text{CoS}_2/\text{MoS}_2$ possessed strong anti-anion interference ability [46]. Humic acid (HA) as the natural organic matter (NOM) had an obvious inhibitory effect on the degradation experiments, attributed to HA capturing SO_4^{2-} and $\cdot\text{OH}$ free radicals and competing with HSO_5^- and SMT for active sites and adsorption sites on the $\text{CoS}_2/\text{MoS}_2$ surface [26,47]. Fig. S3d showed that the presence of different cations (Na^+ , Mg^{2+} and Ca^{2+}) had inhibitory effect on the reaction, which might be attributed to the catalyst aggregation caused by the introduction of cations [34]. The removal efficiencies of SMT in different water matrixes, including tap water, municipal wastewater (influent) without organic compounds (#1 sample, municipal wastewater-TDS) and municipal wastewater with organic compounds (#2 sample, municipal wastewater-TDS-COD) were still more than 90% (Fig. 4i), and their water quality parameters were presented in Tables S3 and S4 [21,48]. Above all, the removal efficiencies could still be over 85% with the addition of most external factors, indicating that the confined system had strong anti-interference ability.

3.3. Determination of major ROS

Typical quenching tests were carried out in different systems to confirm the dominant ROS generation during PMS activation. Tertbutyl alcohol (TBA), ethanol (EtOH), and L-histidine were used as $\cdot\text{OH}$, SO_4^{2-} and $\cdot\text{OH}$, and ${}^1\text{O}_2$ scavengers (Figs. 5a and S4) [49–51]. TBA had almost no inhibitory effect on the degradation of SMT. The reaction rate

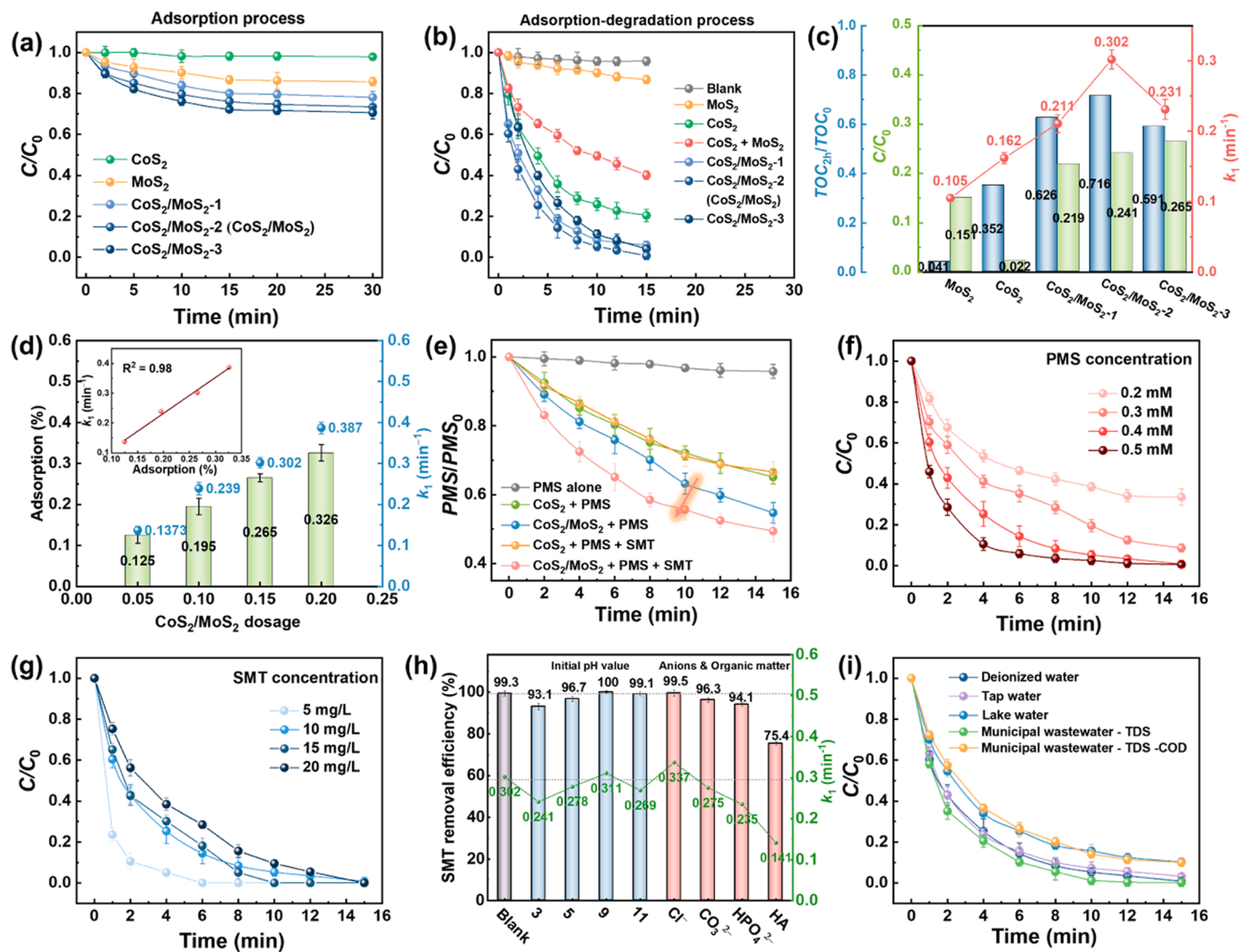


Fig. 4. (a) Adsorption curves of SMT in different catalysts. (b) Removal curves of SMT and (c) TOC removal rate, SMT adsorption amount and degradation rate constant in different systems. (d) The relationship between adsorption rates and k_1 of SMT under different $\text{CoS}_2/\text{MoS}_2$ dosages. (e) PMS consumption in different systems. The influence of (f) PMS and (g) SMT concentration on SMT degradation in the $\text{CoS}_2/\text{MoS}_2/\text{PMS}$ system. (h) The initial value, anion and (i) different water quality on the SMT degradation in $\text{CoS}_2/\text{MoS}_2/\text{PMS}$ systems. Reaction conditions: [catalyst] = 0.15 g/L, [PMS] = 0.4 mM, [SMT] = 10 mg/L, [anions] = 10 mM, [HA] = 10 mg/L, $T = 25 \pm 2^\circ\text{C}$, initial pH = 7.0 \pm 0.2.

constants of SMT with SO_4^{2-} and $\bullet\text{OH}$ ($k_{\text{SO}_4^{2-}, \bullet\text{OH}} = 3.58 \times 10^{10} \text{ M}^{-1}\text{S}^{-1}$, $k_{\bullet\text{OH}, \text{SMT}} = 8.81 \times 10^9 \text{ M}^{-1}\text{S}^{-1}$) determined that the contribution of SO_4^{2-} was much higher than that of $\bullet\text{OH}$ [50]. In the CoS_2/PMS system, only L-histidine almost terminated the SMT degradation, and the same phenomenon occurred in the $\text{CoS}_2 + \text{MoS}_2/\text{PMS}$ system (Fig. S4). The results indicated that $\text{CoS}_2 + \text{MoS}_2$ was a physical contact catalyst, and the degradation mechanism of the $\text{CoS}_2 + \text{MoS}_2/\text{PMS}$ system was consistent with that of CoS_2 with PMS activation ability. In the $\text{CoS}_2/\text{MoS}_2/\text{PMS}$ system, EtOH had the most obvious inhibitory effect, which revealed that SO_4^{2-} might be the main ROS in the $\text{CoS}_2/\text{MoS}_2/\text{PMS}$ system. Meanwhile, the degradation experiments in D_2O showed that ${}^1\text{O}_2$ dominated the SMT degradation in the CoS_2/PMS system, rather than in the $\text{CoS}_2/\text{MoS}_2/\text{PMS}$ system [52]. To more obviously exhibit the alteration of main ROS before and after the formation of interface, k_1 values of quenching tests were employed to estimate the different ROS contributions during the SMT oxidation process (Fig. 5b) [53]. Specifically, the contribution of SO_4^{2-} substantially elevated in the $\text{CoS}_2/\text{MoS}_2/\text{PMS}$ system compared with the CoS_2/PMS system, declaring that Co at the interface might be the new active site produced by SO_4^{2-} to accelerate the SMT degradation. In addition, quantitative experiments (Fig. 5c) showed that only the amount of SO_4^{2-}

significantly increased after forming interface, which validated the results of quenching tests [6].

Electron paramagnetic resonance (EPR) analysis by using 2,2,6,6-tetramethylpiperidine (TEMP) and 5,5-dimethyl-2-pyrrolidone-N-oxyl (DMPO) as trapping agents was another method to validate valid ROS (Fig. 5d-e). The signals of DMPO- $\bullet\text{OH}$, DMPO- SO_4^{2-} , and TEMP- ${}^1\text{O}_2$ were not displayed in the PMS alone system which was considered as the blank contrast. To explore the pathway of ${}^1\text{O}_2$ generation, DMPO was used as a trapping agent for superoxide radicals (O_2^{2-}). Fig. S5a-b showed that the addition of DMPO led to a dramatic decrease in the ESR signal intensity of the TEMP- ${}^1\text{O}_2$ adduct in the $\text{CoS}_2/\text{MoS}_2/\text{PMS}/\text{TEMP}$ system to almost disappear. Meanwhile, the O_2^{2-} was captured by DMPO in methanol, the signal of DMPO- O_2^{2-} almost disappeared under N_2 atmosphere compared with that under air condition, indicating that ${}^1\text{O}_2$ originated from the stepwise conversion of dissolved oxygen [54]. Therefore, p-benzoquinone (p-BQ) was used to quench O_2^{2-} in the $\text{CoS}_2/\text{MoS}_2/\text{PMS}$ system. Fig. S5c indicated that the degradation efficiency of SMT decreased slightly in which the inhibition rate was much lower than that of EtOH, indicating that SO_4^{2-} was the most dominant ROS in the $\text{CoS}_2/\text{MoS}_2/\text{PMS}$ system. The intensity of DMPO- $\bullet\text{OH}$ and DMPO- SO_4^{2-} signals in the $\text{CoS}_2/\text{MoS}_2/\text{PMS}$ system experienced an

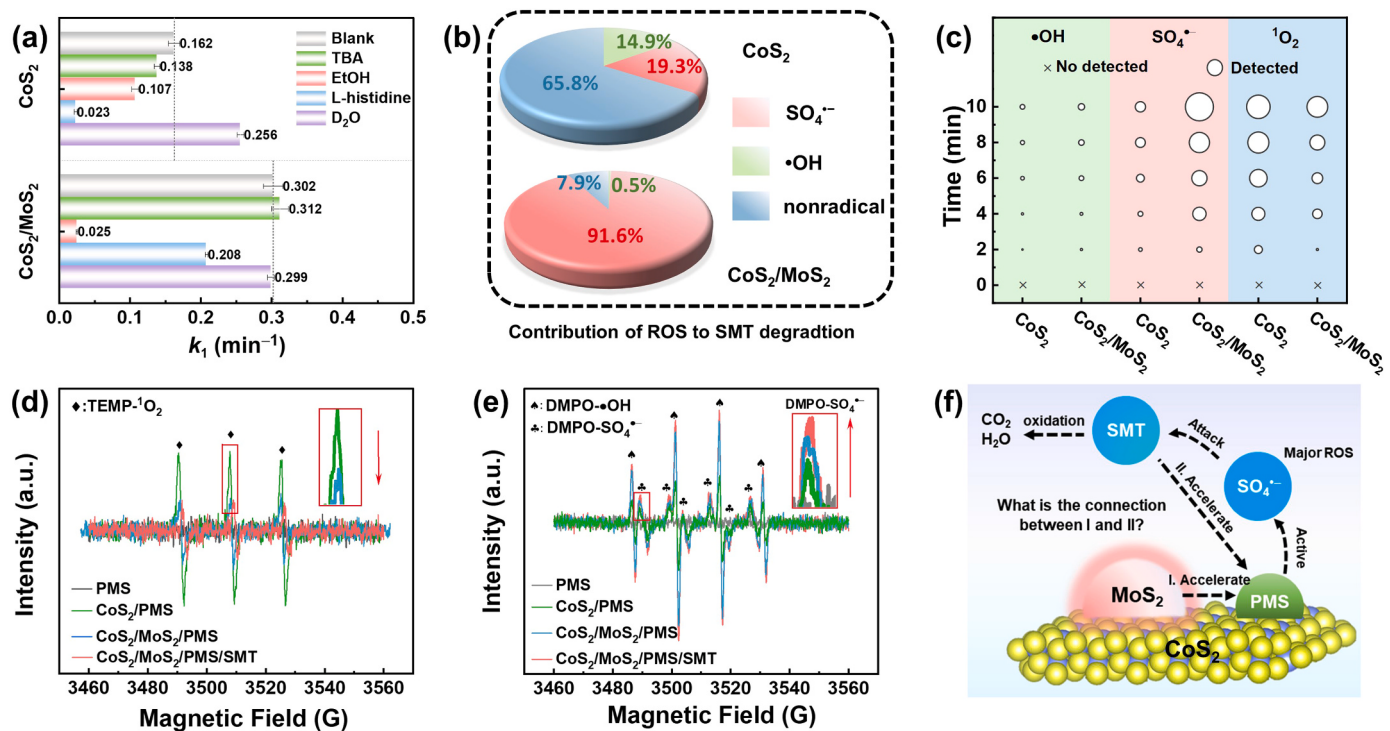


Fig. 5. (a) k_1 of SMT degradation in the presence of different scavengers and D₂O in CoS₂/PMS and CoS₂/MoS₂/PMS systems. (b) ROS contribution in CoS₂/PMS and CoS₂/MoS₂/PMS systems. (c) Quantitative analyses of •OH, SO₄^{•-}, and ¹O₂ present in CoS₂/MoS₂/PMS system. EPR spectra at 3 min using (d) TEMP and (e) DMPO in different systems. (f) Radical generation route in CoS₂/MoS₂.

increasing trend than those in CoS₂/PMS system, and the changing trend of the TEMP-¹O₂ signal was opposite [53], which were consistent with ROS quantitative experiments. Furthermore, the addition of SMT increased the DMPO-SO₄^{•-} signal strength at the same reaction time (3 min), which might be attributed to the electronic transfer effect between organic pollutants and catalysts through electrostatic, hydrogen bonding, and other interactions [55]. In brief, SMT and MoS₂ in CoS₂/MoS₂ might promote SO₄^{•-} radical production in the confined Fenton-like reaction (Fig. 5f).

3.4. Uncovering the origin of the enhanced catalytic performance

3.4.1. The effect of interface electronic reconfiguration on PMS activation

To explore the main reasons for the highly efficient SMT degradation, the interfacial electronic behaviors of catalysts were investigated using XPS. Attributing to the almost no SMT adsorption on the CoS₂ surface, the XPS results before and after reaction in the CoS₂/PMS activation system were compared to judge the modification advantages of MoS₂ on Co active site to exclude the influence of SMT on CoS₂/MoS₂ (Fig. S6), which was detailed in Text S9. The contents of different ions' states were calculated from the relative peak areas of XPS. The XPS results before and after reaction declared that the oxidation degree of CoS₂ was significantly higher than that of CoS₂/MoS₂, but the degradation ability of CoS₂ was significantly lower compared with CoS₂/MoS₂ in the activation system. Therefore, it was speculated that the electrons stored at the interface of MoS₂ in CoS₂/MoS₂ could regress to the active site at the right time to accelerate PMS activation. DFT calculation was utilized to further reveal the changes of interface active site from the atomic level [56]. The density of states (DOS) of CoS₂/MoS₂ at the Fermi level was significantly higher than that of pure CoS₂ and MoS₂ (Fig. S7) [57], indicating that the interface between CoS₂ and MoS₂ was conducive to improving the electrical conductivity of the catalyst, which was consistent with the results of EIS and Tafel polarization curve (Fig. S8) [58], which was detailed in Text S10. To better understand the interface electronic structure reconfiguration, the projected DOS (PDOS) of Co

d orbital in CoS₂ and CoS₂/MoS₂ was obtained (Fig. 6a-c). For pure CoS₂, the divalent Co²⁺ cations located at the center of the CoS₆ octahedron, and the electronic configuration of Co 3d orbital was t_{2g}⁶e_g¹. The single electron on the Co-d_{x²-y²} orbital at the interface of CoS₂/MoS₂ transferred to MoS₂ to form a new electronic configuration t_{2g}⁶e_g⁰, which signified that Co at the interface changed from Co²⁺ to Co³⁺ after electron transfer, consistent with the previous XPS and XAFS results. The creation of more Co³⁺ (t_{2g}⁶e_g⁰) at the interface rendered CoS₂/MoS₂ abundant zero-filling e_g orbitals to strongly adsorb PMS [3].

The adsorption energy (E_{ads}) capacity of CoS₂ for PMS (-0.96 eV) was obviously weaker than that of CoS₂/MoS₂ (-1.38 eV) (Fig. 6d). The number of electrons transferred to PMS (Q) and the O–O bond length of PMS* (l_{O-O}) declared that the CoS₂ and CoS₂/MoS₂ could serve as the electron donor for PMS decomposition [59]. The Q and l_{O-O} transferred from CoS₂ (0.629 e, 1.467 Å) were lower than CoS₂/MoS₂ (0.789 e, 1.481 Å), revealing that CoS₂/MoS₂ not only had stronger adsorption capacity, but also had stronger activation capacity than CoS₂. The PDOS of Co 3d and Mo 4d orbitals in CoS₂/MoS₂ before and after PMS adsorption (Fig. S9) declared that the electrons might be regressed from MoS₂ side to CoS₂ during PMS activation, and finally provided to PMS to promote the SO₄^{•-} generation [60]. The transition state (TS) search method was used to investigate the fracture of the O–O bond on the CoS₂ and CoS₂/MoS₂ models to further explain the process of SO₄^{•-} generation (Fig. 6e). The reaction barrier of TS generation and the dissociation energy of SO₄^{•-} on the CoS₂/MoS₂ surface (0.28 and 3.68 eV) were significantly lower than CoS₂ (0.56 and 4.02 eV). In summary, the special interface could store and supply electrons to enhance the PMS adsorption and activation ability of CoS₂/MoS₂.

3.4.2. The effect of SMT enrichment on PMS activation

The XPS results of fresh and used CoS₂/MoS₂ in three systems (adsorption, activation and degradation systems) was used to further reveal the function of the confined nanoreactor caused by SMT (Fig. 7a-c). In the adsorption system with only SMT added, the peak positions of Co 2p, Mo 3d, and S 2p in the used CoS₂/MoS₂ (SMT) shifted to lower

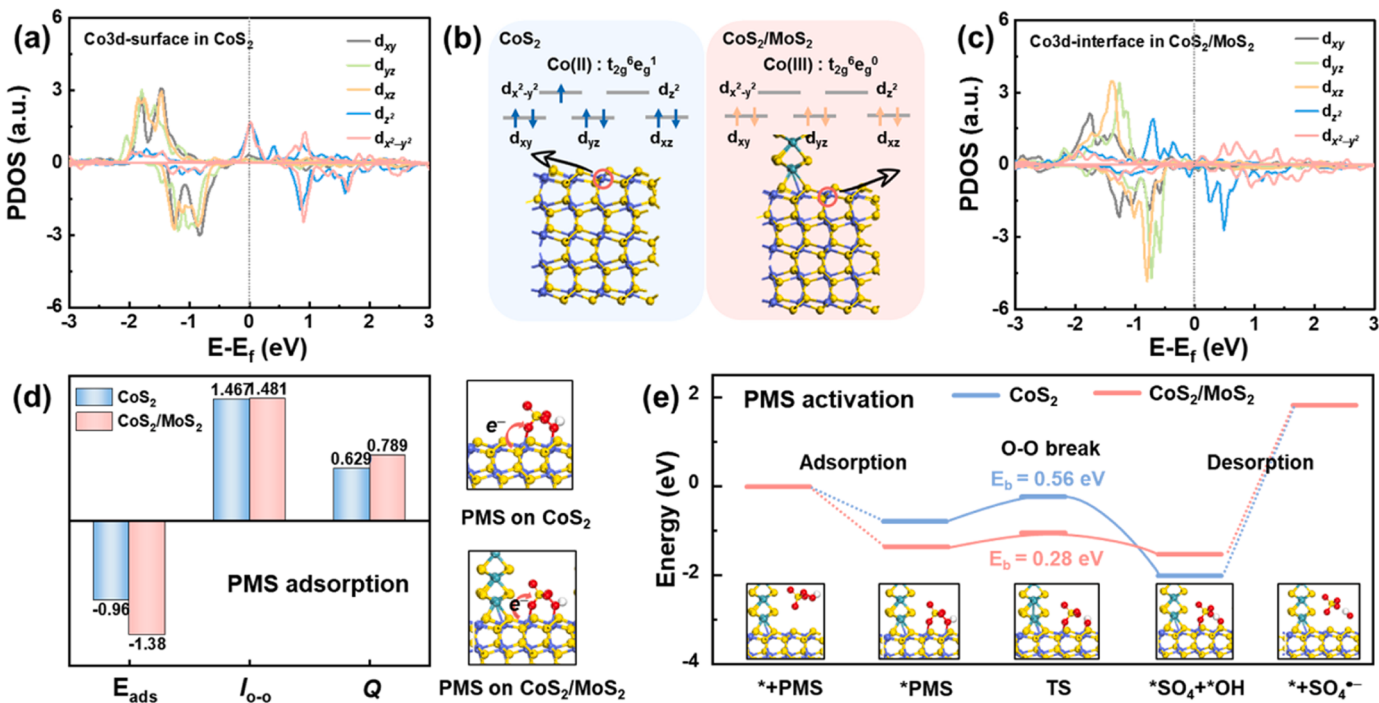


Fig. 6. (a) PDOS of Co 3d in CoS_2 . (b) Schematic of Co 3d orbital electron distribution in CoS_2 and $\text{CoS}_2/\text{MoS}_2$. (c) PDOS of Co 3d in $\text{CoS}_2/\text{MoS}_2$. (d) Adsorption configuration of HSO_4^- on the surface of CoS_2 and $\text{CoS}_2/\text{MoS}_2$ models. (e) Reaction path of PMS activation and energy profile of SO_4^- generation process (inset corresponding intermediate structures).

energy levels by 0.8, 0.5, and 0.1 eV compared to those in the fresh $\text{CoS}_2/\text{MoS}_2$. The relative peak area of Co^{2+} increased slightly by 2.6% and S-SO_4^{2-} decreased by 3.9%. These results revealed that the interaction between $\text{CoS}_2/\text{MoS}_2$ and SMT would donate electrons to the adsorption sites, resulting in a decreased metal ion oxidation state [61]. In the activation system with only PMS added, the peaks at 236.1 eV and 233.6 eV attributed to the $\text{Mo}^{6+} 3d_{3/2}$ and $\text{Mo}^{6+} 3d_{5/2}$ were appeared, which indicated that part of Mo^{4+} in the used $\text{CoS}_2/\text{MoS}_2$ (PMS) was oxidized to generate Mo^{6+} [62]. The results of shifts in peak positions (shifted to higher energy levels 0.1, 0.3, and 0.1 eV) and changes in relative peak areas (5.0% of Co^{2+} converted to Co^{3+} , 18.2% of Mo^{4+} converted to Mo^{6+} and 2.0% of S-SO_4^{2-} generated) after the reaction were opposite to the adsorption system, indicating that the interaction between $\text{CoS}_2/\text{MoS}_2$ and PMS would consume electrons from the $\text{CoS}_2/\text{MoS}_2$ [63]. In the degradation system with both SMT and PMS added, the oxidation degrees of Co 2p, Mo 3d, and S 2p in the used $\text{CoS}_2/\text{MoS}_2$ (SMT+PMS) became lower (1.4% of Co^{2+} converted to Co^{3+} , 11.3% of Mo^{4+} converted to Mo^{6+} and 1.9% of S-SO_4^{2-} decreased) compared with used $\text{CoS}_2/\text{MoS}_2$ (PMS), and the peak positions hardly changed. In addition, the relative content of edge S in MoS_2 decreased in adsorption and degradation systems, indicating that edge S sites might be related to SMT adsorption [26]. Therefore, SMT adsorbed on MoS_2 might supply electron to accelerate the electron transfer during PMS activation to give the $\text{CoS}_2/\text{MoS}_2$ excellent activation ability, which was consistent with EPR results.

The FTIR spectra of SMT, fresh MoS_2 , fresh $\text{CoS}_2/\text{MoS}_2$, used MoS_2 , and used $\text{CoS}_2/\text{MoS}_2$ in the adsorption system were shown in Fig. 7d. The spectra of fresh MoS_2 and $\text{CoS}_2/\text{MoS}_2$ displayed that the absorption peaks at 3400, 1704, 1103, and 632 cm^{-1} were attributed to the stretching vibration of -OH, C=O in adsorbed CO_2 on catalysts surface, the oxidation of sulfur specie and metal-S bonds [64], respectively. After the MoS_2 and $\text{CoS}_2/\text{MoS}_2$ underwent the adsorption process, the spectra of used MoS_2 and $\text{CoS}_2/\text{MoS}_2$ clearly appeared part of the characteristic peaks of SMT containing 3300–3200, 1550–1350, 1150, and 900 – 650 cm^{-1} which were attributed to the stretching vibration of $-\text{NH}_2$, backbone vibrations of pyrimidine and phenyl rings, sulfonyl

groups, and aromatic hydrogen of benzene ring, [65] respectively. The above results indicated that $\text{CoS}_2/\text{MoS}_2$ could adsorb SMT to achieve pollutant enrichment. Intuitive verification of the electronic interaction between SMT and $\text{CoS}_2/\text{MoS}_2$ was carried out by using electrochemical characterization tests. The electrochemical impedance of the catalysts was significantly reduced when PMS and SMT were added simultaneously (Fig. 7e), indicating that the presence of SMT would significantly increase the electron transfer rate of the $\text{CoS}_2/\text{MoS}_2/\text{PMS}$ system. Meanwhile, chronoamperometry test (i-t) declared that the current density increased obviously when SMT was added first, and then the current density decreased obviously after PMS was added, in which the decrease amplitude was 0.36 mA higher than that (0.30 mA) in the PMS first added system (Fig. 7f). This declared that the presence of SMT might induce the electron transfer potential to become lower on the $\text{CoS}_2/\text{MoS}_2$ surface and then accelerate the reaction between PMS and $\text{CoS}_2/\text{MoS}_2$ [49]. In summary, the confined $\text{CoS}_2/\text{MoS}_2$ nanoreactor could enrich SMT in confined space to shorten free radical migration and might mediate the electrons provided by SMT adsorbed on the surface to improve the electron transfer ability of $\text{CoS}_2/\text{MoS}_2$, ultimately promoting SMT degradation.

Based on the experimental, characterization, and theoretical results, the mechanism for the enhancement of catalytic activity via confined $\text{CoS}_2/\text{MoS}_2$ nanoreactor was unveiled (Fig. 7g). PMS activation in the traditional Co-based system is achieved by the transition between $\text{Co}^{2+}/\text{Co}^{3+}$ (left of Fig. 7g). The confined nanoreactor could both mediate the transportation of SMT electrons and regress electrons from interface reconfiguration to the interfacial Co sites in the $\text{CoS}_2/\text{MoS}_2/\text{PMS}$ system (right of Fig. 7g). The multi-source electron input could accelerate PMS activation to promote SO_4^\bullet generation [55,66], and MoS_2 as the traditional cocatalyst could achieve valence state cycling of Co ions in the catalyst [24]. Meanwhile, the confined nanoreactor could concentrate SMT in confined space and shorten the transport path of SO_4^\bullet radicals. Ultimately, the confined nanoreactor in the interface-mediated PMS activation system significantly enhanced the degradation performance of SMT.

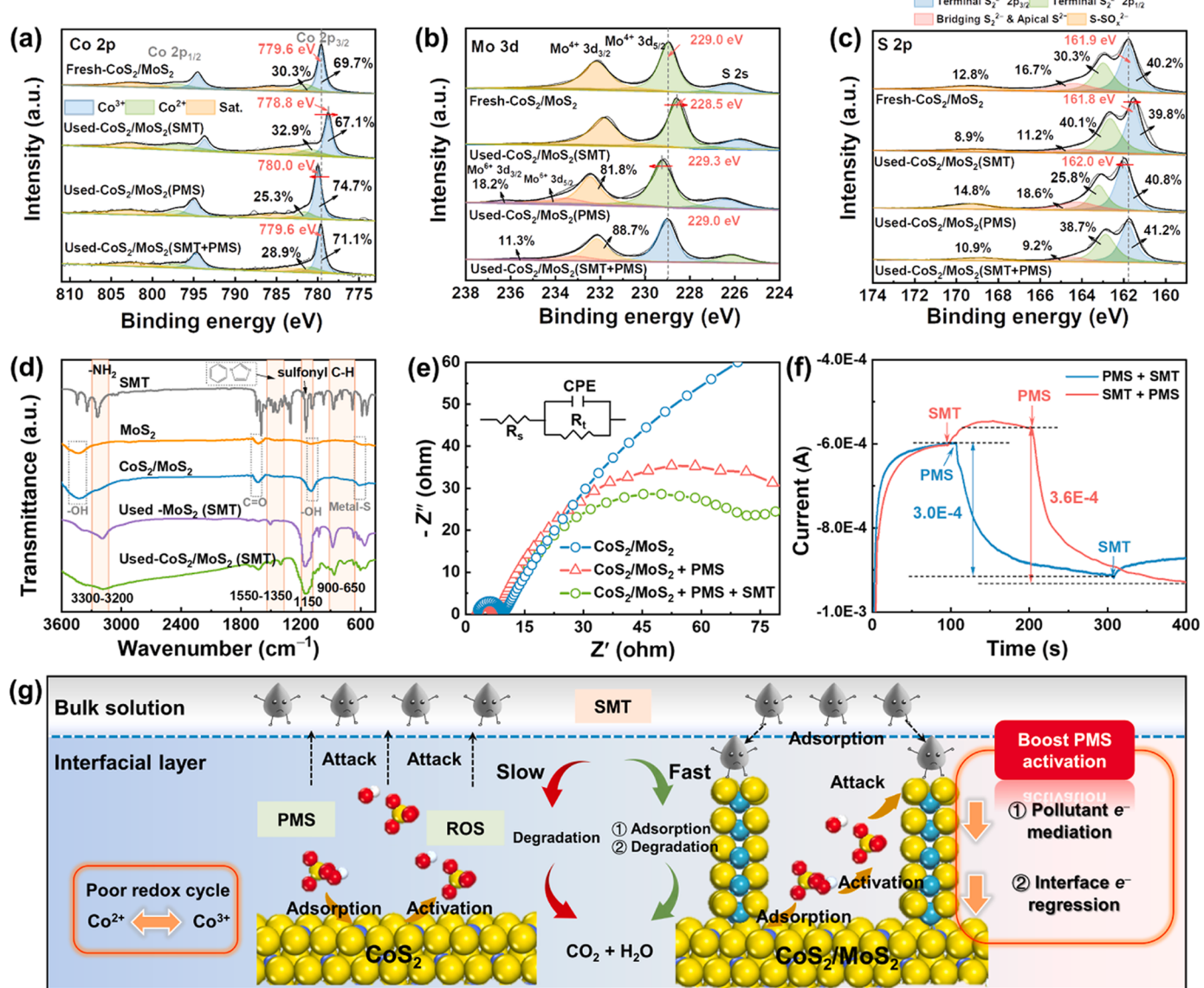


Fig. 7. XPS spectra of Co₃S₂/MoS₂ before and after different reactions: (a) Co 2p, (b) Mo 3d, and (c) S 2p. (d) FT-IR spectra of MoS₂ and Co₃S₂/MoS₂ before and after different reactions. (e) EIS of Co₃S₂/MoS₂ in different electrolytes. (f) *i-t* of Co₃S₂/MoS₂ react with SMT and PMS. (g) Schematic illustration of enhanced SMT degradation via the confined nanoreactor.

3.5. Radical-dominated degradation pathways

DFT calculations were used to predict the attack sites of SMT from an electronic perspective. Fig. 8a displayed the structural formula and atomic types of SMT. The Highest Occupied Molecular Orbital (HOMO) of SMT indicated that the –NH₂ group, –NH–SO₂– group, and benzene ring in SMT were susceptible to ROS (SO₄²⁻, •OH, and ¹O₂) attacks (Fig. 8b). In order to, Multiwfn software was used to accurately predict reaction sites via calculating the Fukui function (f^0 and f^-) of SMT (Fig. S10), where atoms with higher f^- values (N23, C13, C4, N8, C18, and C16) were more susceptible to ¹O₂ attack, while atoms with higher f^0 values (N23, N6, C5, C3, C20, and C4) could indicate the regioselectivity of free radicals (SO₄²⁻ and •OH) [67]. N23 with highest f^0 and f^- values had the most vulnerable site during the degradation process. The •OH and SO₄²⁻ radicals could react with organic compounds via single-electron transfer, radical adduct formation, and hydrogen abstraction. ¹O₂ could react with organic compound via single-electron transfer and electrophilic addition. Combined with the results of the intermediate after SMT oxidation detected by LC-MS analysis, the

possible degradation pathways of SMT in the Co₃S₂/PMS system were proposed (Fig. 8c). In pathway I, P1 was converted from SMT via –OH addition by •OH [68]. P1 would transfer to P2 via single-electron transfer, hydroxylation, and hydrogen abstraction by all types ROS. –NH–SO₂– group in P2 was attacked by •OH and SO₄²⁻ radicals via single-electron transfer, resulting in S–N bond cleavage and the formation of P3 and P4. In pathway II, SMT underwent heterocyclic ring-opening reaction via single-electron transfer by all types ROS to generate P5. The groups on the benzene ring in P5 are replaced by •OH to generate P6 [69]. In pathway III, the products P3 and P7 were generated from the S–N bond cleavage in SMT by single or synergistic attacks of SO₄²⁻, •OH, and ¹O₂, respectively. P7 would undergo C–S cleavage or •OH substitution to form P6 or P8. In pathway IIII, SMT underwent smile rearrangement to generate products P9 and P10, which was initiated by an aniline radical cation of SMT via an electron transfer mechanism [5]. P10 occurred C–N bond cleavage reaction to generate P3 and P4. Due to the single electron transfer reaction between ROS and organic compounds, the ring opening of the benzene ring and heterocyclic ring led to the formation of P11, P12, P13, and P14. Ultimately,

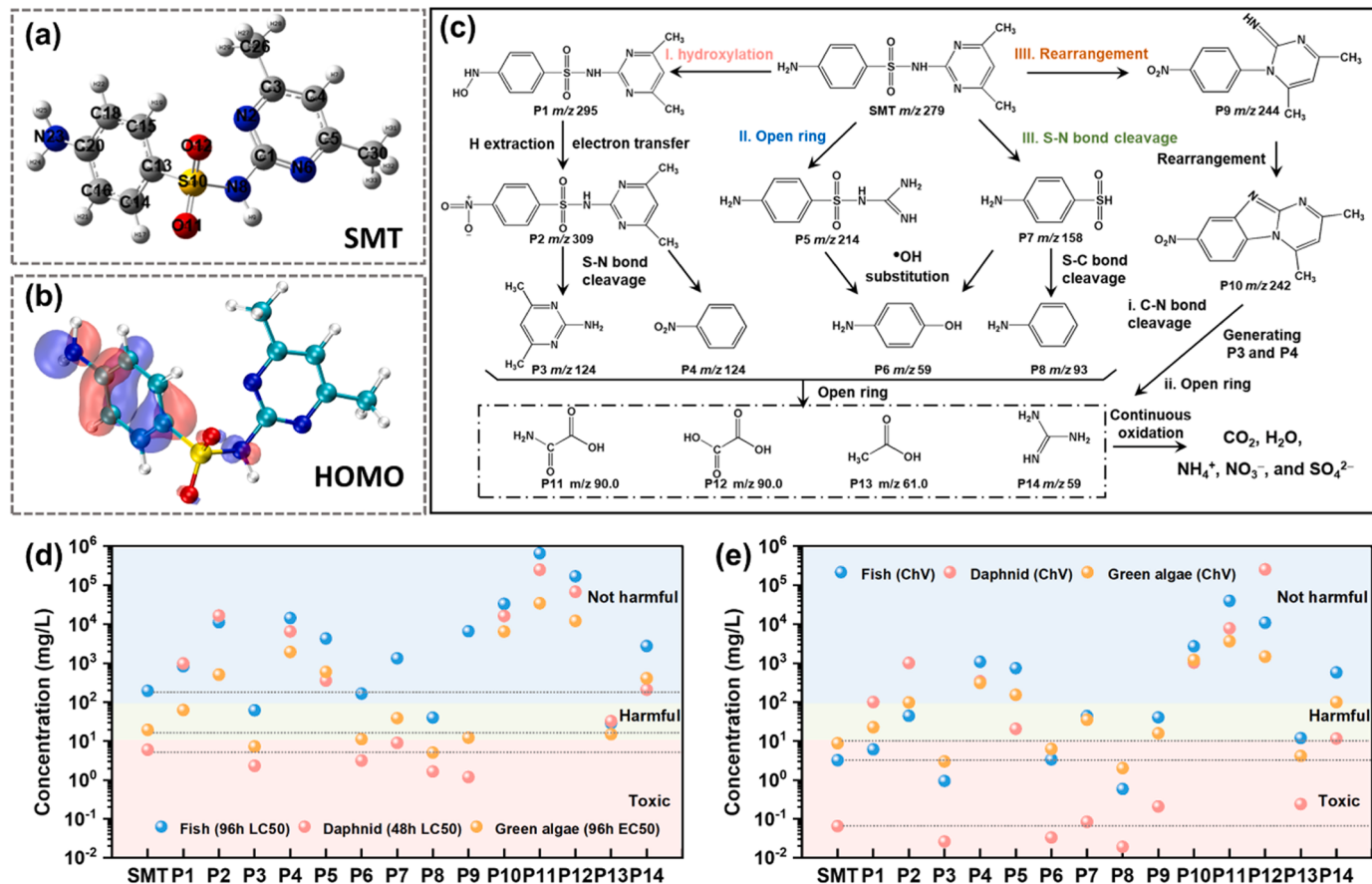


Fig. 8. (a) The structure of SMT. (b) The molecular orbital electron densities HUMO of SMT. (c) The proposed degradation pathway of SMT in the $\text{CoS}_2/\text{MoS}_2/\text{PMS}$ system. (d) Acute toxicity and (e) chronic toxicity for fish, daphnid, and green algae.

SMT is finally completely mineralized to CO_2 and H_2O over time via the synergistic effect of SO_4^{2-} , $\bullet\text{OH}$, and ${}^1\text{O}_2$. The ecological structure activity relationship (ECOSAR) program was used to predict the acute (short term) and chronic (long term or delayed) toxicity of SMT and its intermediates to fish, daphnid, and green algae [49]. Fig. 8d and e indicated that the toxicity of most intermediates (except for P3, P6, P8, and P9) was significantly lower than that of SMT. However, SMT would be gradually evolved into small molecules, even CO_2 and H_2O within 3 h under SO_4^{2-} -dominated degradation mechanism. Therefore, the $\text{CoS}_2/\text{MoS}_2/\text{PMS}$ system had detoxification function for SMT pollutants in water.

3.6. Evaluation of catalytic stability and practicality

ICP-OES results showed that the leaching amounts of Co and Mo ions were 0.06 and 0.10 mg/L during the PMS activation by $\text{CoS}_2/\text{MoS}_2$, which was much lower than the permissible limit (1 mg/L) given by the Chinese National Standard (GB 25467–2010) [49]. Homogeneous experiments suggest that leached Co ions were not significant for the degradation of SMT in the $\text{CoS}_2/\text{MoS}_2/\text{PMS}/\text{SMT}$ reaction, demonstrating that the SMT degradation in the $\text{CoS}_2/\text{MoS}_2/\text{PMS}$ system followed a multiphase catalytic pathway (Fig. S11). The presence of MoS_2 slightly accelerated the degradation of SMT compared to the $\text{Co}^{2+}/\text{PMS}$ system, but the degradation rate of SMT in the $\text{Co}^{2+}+\text{MoS}_2/\text{PMS}$ system was much lower than that in the $\text{CoS}_2/\text{MoS}_2/\text{PMS}$ system (Fig. S11). Therefore, we speculated that the accelerated reduction of trace cobalt ions by MoS_2 was not the dominant degradation mechanism in the $\text{CoS}_2/\text{MoS}_2/\text{PMS}$ system. The Co ion leaching in CoS_2/PMS system (1.25 mg/L) was obviously higher than the $\text{CoS}_2/\text{MoS}_2/\text{PMS}$ system, indicating that MoS_2 could effectively protect the active components

against rundown due to optimizing the structure of interface active sites through the covalent bonds of Co–S–Mo. $\text{CoS}_2/\text{MoS}_2$ had highly reusable in eight consecutive cycles with nearly constant SMT removal efficiency (above 93%), but CoS_2 only could remove 39.9% SMT in eighth cycle process (Fig. 9a). Apart SMT, the $\text{CoS}_2/\text{MoS}_2/\text{PMS}$ system had excellent removal ability for other drugs, including sulfonamides (SA), sulfamethoxazole (SMX), sulfathiazole (STZ), and sulfamerazine (SMR)), ofloxacin (OFX), tetracycline (TC) and acetaminophen (APAP) (Fig. 9b). These results indicated that the confined $\text{CoS}_2/\text{MoS}_2$ nanoreactor via Co–S–Mo bond could significantly reduce Co leaching and synchronously enhance catalytic stability and reactivity.

The $\text{CoS}_2/\text{MoS}_2/\text{PMS}$ system was used to degrade a real medical wastewater (sampling point is a hospital in Liaoning Province, China) containing various pollutants such as drugs, disinfectants, diagnostic reagents, parasitic eggs, detergents and many viruses to evaluate its potential application in real water environments. Three-dimensional excitation-emission matrix (3D-EEM) fluorescence spectra of actual medical wastewater before and after (30 min) the reaction in the $\text{CoS}_2/\text{MoS}_2/\text{PMS}$ system displayed that the fluorescence intensity of 280.0/340.0 (Peak A), 225.0/335.0 (Peak B) and 325.0/415.0 (Peak C) weakened after the reaction (Fig. 9c and d), in which Peak A and B were related to aromatic proteins such as tyrosine and Peak C was attributed to humic acid-like organics [2,70]. The results indicated that this system could effectively remove aromatic organic matter and humic acid-like organics from real medical wastewater. Meanwhile, the decrease in total organic carbon (TOC), chemical oxygen demand (COD), and biological oxygen demand (BOD), especially the increase in BOD/COD (B/C) ratio from 0.34 to 0.61 (Fig. S12) after actual hospital wastewater treatment in $\text{CoS}_2/\text{MoS}_2/\text{PMS}$ system, indicated a significant improvement in hospital wastewater quality after treatment. ICP-OES results

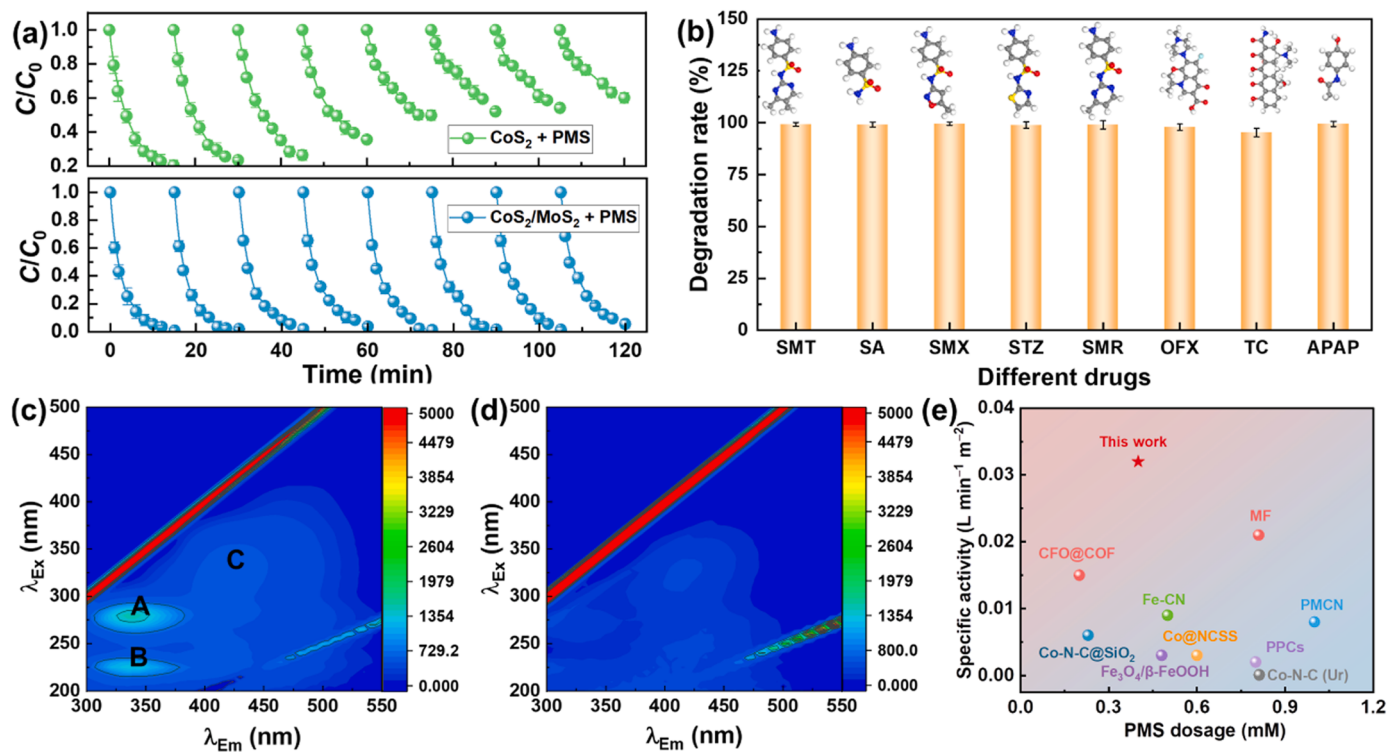


Fig. 9. (a) SMT removal efficiency over eight cycles under different systems. (b) Different drug degradation rates in $\text{CoS}_2/\text{MoS}_2/\text{PMS}$ system. 3D-EEM fluorescence spectra of the actual medical wastewater (c) before and (d) after purification in $\text{CoS}_2/\text{MoS}_2/\text{PMS}$ system. (e) Comparison of intrinsic catalytic activity of the $\text{CoS}_2/\text{MoS}_2$ with other reported catalysts in literature for PMS activation. Reaction conditions: [catalyst] = 0.15 g/L, [PMS] = 0.4 mM, [drugs] = 10 mg/L, [anions] = 10 mM, T = $25 \pm 2^\circ\text{C}$, initial pH = 7.0 ± 0.2 .

showed that the Co leaching concentration of actual medical wastewater after $\text{CoS}_2/\text{MoS}_2/\text{PMS}$ system treatment was 0.09 mg/L, which was much lower than the permissible limit (1 mg/L) given by the Chinese National Standard (GB 25467–2010) [49]. In addition, attributed to the special interface structure, $\text{CoS}_2/\text{MoS}_2$ exhibited extraordinary PMS activation activity to achieve high-speed sulfonamides degradation at fewer PMS concentration than most catalysts (Fig. 9e and Table S5). The above results indicated that the $\text{CoS}_2/\text{MoS}_2/\text{PMS}$ system had excellent remediation ability for real medical wastewater.

4. Conclusion

This work proposed an enhanced mechanism of interface-mediated PMS activation on catalytic activity and reaction stability in the Fenton-like reaction, and emphasized the crucial role of interfacial covalent bond (Co–S–Mo) in building the confined nanoreactor. Concretely, this work divided the SMT degradation process into two steps: (1) SMT adsorption process. The vertical stacking manner could facilitate the MoS_2 edge exposure to provide adsorption sites (edge S) in the confined nanoreactor, which could concentrate SMT in a confined space and mediated electron transport from SMT to the active sites; (2) PMS activation process. Co-containing e_g empty orbitals at the active interface served as the PMS optimal activation site due to interfacial electronic reconstruction of vertical interface, and MoS_2 returned the obtained interfacial electrons to the active sites during the PMS activation. The multisource electron input process could trigger faster electron transfer into PMS for $\text{SO}_4^{\bullet-}$ radicals generation, and the surface-confined reaction could reduce the transport distance of $\text{SO}_4^{\bullet-}$ radicals. The unique catalytic pathway would break the limitations caused by the poor Co redox cycling in traditional PMS activation systems to realize efficient, stable, and sustained SMT degradation. The experiments showed that $\text{CoS}_2/\text{MoS}_2/\text{PMS}$ system could facilitate a rapid SMT degradation rate of 0.302 min^{-1} and exhibited excellent acid-base

resistance and good purification performance for actual medical wastewater. In addition, choosing appropriate support materials to load $\text{CoS}_2/\text{MoS}_2$ could resolve the Co-based catalysts faced many challenges in practical applications, especially their production costs and service life. Above all, our findings provided a novel and rigorous understanding of the catalytic mechanism enhanced via vertical interface structure; besides, the adsorption between catalysts and contaminants was associated with self-removal, and the influence of contaminants' characteristics on the removal process should be further explored to achieve targeted removal of other toxic contaminants from the aquatic environment.

CRediT authorship contribution statement

Hu Bin: Visualization, Validation, Conceptualization. **Liu Ji:** Software, Resources. **Li Jihong:** Resources, Project administration. **Xia Yuangu:** Writing – review & editing, Data curation. **Zhang Lin:** Supervision, Methodology. **Fang Zhimo:** Methodology, Investigation, Formal analysis, Conceptualization. **Wang Lidong:** Writing – review & editing, Funding acquisition. **Li Kai:** Supervision, Methodology. **Lu Qiang:** Writing – review & editing, Visualization, Resources, Funding acquisition.

Declaration of Competing Interest

The authors declare that they have no known competing financial interests or personal relationships that could have appeared to influence the work reported in this paper.

Data availability

Data will be made available on request.

Acknowledgments

This work was financially supported by the Postdoctoral Fellowship Program of CPSF (No. GZB20230207), National Natural Science Foundation of China (No. 52276189), Fundamental Research Funds for the Central Universities (No. 2023JC009, 2022YQ002), and the National Science Fund for Distinguished Young Scholars (No. 52325004). The authors would like to thank ECOSAR software supplied by the U.S. Environmental Protection Agency.

Appendix A. Supporting information

Supplementary data associated with this article can be found in the online version at [doi:10.1016/j.apcatb.2024.123769](https://doi.org/10.1016/j.apcatb.2024.123769).

References

- [1] M. Lamba, D.W. Graham, S.Z. Ahammad, Hospital wastewater releases of carbapenem-resistance pathogens and genes in urban India, *Environ. Sci. Technol.* 51 (2017) 13906–13912, <https://doi.org/10.1021/acs.est.7b03380>.
- [2] Z.H. Xie, C.S. He, Y.L. He, S.R. Yang, S.Y. Yu, Z.K. Xiong, Y. Du, Y. Liu, Z.C. Pan, G. Yao, B. Lai, Peracetic acid activation via the synergic effect of Co and Fe in CoFe-LDH for efficient degradation of pharmaceuticals in hospital wastewater, *Water Res.* 232 (2023) 119666, <https://doi.org/10.1016/j.watres.2023.119666>.
- [3] Z.Y. Guo, Y. Si, W.Q. Xia, F. Wang, H.Q. Liu, C. Yang, W.J. Zhang, W.W. Li, Electron delocalization triggers nonradical Fenton-like catalysis over spinel oxides, *Proc. Natl. Acad. Sci.* 119 (2022) e2201607119, <https://doi.org/10.1073/pnas.2201607119>.
- [4] X. Xu, Y. Zhang, Y. Chen, C. Liu, W. Wang, J. Wang, H. Huang, J. Feng, Z. Li, Z. Zou, Revealing *OOH key intermediates and regulating H₂O₂ photoactivation by surface relaxation of Fenton-like catalysts, *Proc. Natl. Acad. Sci.* 119 (2022) e2205562119, <https://doi.org/10.1073/pnas.2205562119>.
- [5] Z. He, M. Chen, M. Xu, Y. Zhou, Y. Zhang, G. Hu, LaCo_{0.5}Ni_{0.5}O₃ perovskite for efficient sulfafurazole degradation via peroxymonosulfate activation: Catalytic mechanism of interfacial structure, *Appl. Catal., B* 335 (2023) 122883, <https://doi.org/10.1016/j.apcatb.2023.122883>.
- [6] Q. Zhou, C. Song, P. Wang, Z. Zhao, Y. Li, S. Zhan, Generating dual-active species by triple-atom sites through peroxymonosulfate activation for treating micropollutants in complex water, *Proc. Natl. Acad. Sci.* 120 (2023) e2300085120, <https://doi.org/10.1073/pnas.2300085120>.
- [7] T. An, H. Yang, G. Li, W. Song, W.J. Cooper, X. Nie, Kinetics and mechanism of advanced oxidation processes (AOPs) in degradation of ciprofloxacin in water, *Appl. Catal., B* 94 (2010) 288–294, <https://doi.org/10.1016/j.apcatb.2009.12.002>.
- [8] Z.H. Xie, C.S. He, H.Y. Zhou, L.L. Li, Y. Liu, Y. Du, W. Liu, Y. Mu, B. Lai, Effects of molecular structure on organic contaminants' degradation efficiency and dominant ROS in the advanced oxidation process with multiple ROS, *Environ. Sci. Technol.* 56 (2022) 8784–8795, <https://doi.org/10.1021/acs.est.2c00464>.
- [9] Q. Yi, J. Ji, B. Shen, C. Dong, J. Liu, J. Zhang, M. Xing, Singlet oxygen triggered by superoxide radicals in a molybdenum cocatalytic Fenton reaction with enhanced REDOX activity in the environment, *Environ. Sci. Technol.* 53 (2019) 9725–9733, <https://doi.org/10.1021/acs.est.9b01676>.
- [10] S. Ren, X. Xu, Z.-S. Zhu, Y. Yang, W. Tian, K. Hu, S. Zhong, J. Yi, X. Duan, S. Wang, Catalytic transformation of microplastics to functional carbon for catalytic peroxymonosulfate activation: Conversion mechanism and defect of scavenging, *Appl. Catal., B* 342 (2024) 123410, <https://doi.org/10.1016/j.apcatb.2023.123410>.
- [11] X. Mi, P. Wang, S. Xu, L. Su, H. Zhong, H. Wang, Y. Li, S. Zhan, Almost 100% peroxymonosulfate conversion to singlet oxygen on single-atom CoN₂₊₂ Sites, *Angew. Chem. Int. Ed.* 60 (2021) 4588–4593, <https://doi.org/10.1002/anie.202014472>.
- [12] P. Yang, Y. Long, W. Huang, D. Liu, Single-atom copper embedded in two-dimensional MXene toward peroxymonosulfate activation to generate singlet oxygen with nearly 100% selectivity for enhanced Fenton-like reactions, *Appl. Catal., B* 324 (2023) 122245, <https://doi.org/10.1016/j.apcatb.2022.122245>.
- [13] N. Logeshwaran, S. Ramakrishnan, S.S. Chandrasekaran, M. Vinothkannan, A. R. Kim, S. Sengodan, D.B. Velusamy, P. Varadhan, J.-H. He, D.J. Yoo, An efficient and durable trifunctional electrocatalyst for zinc-air batteries driven overall water splitting, *Appl. Catal., B* 297 (2021) 120405, <https://doi.org/10.1016/j.apcatb.2021.120405>.
- [14] T. Shishidou, A.J. Freeman, R. Asahi, Effect of GGA on the half-metalllicity of the itinerant ferromagnet CoS₂, *Phys. Rev. B* 64 (2001) 180401, <https://doi.org/10.1103/PhysRevB.64.180401>.
- [15] J.-Y. Zhao, J.-M. Zhang, Half-metallic properties of CoS₂, doped Co_{0.25}S_{1.75} and Co_{0.25}S_{1.75}, *Mater. Res. Express* 4 (2017) 086306, <https://doi.org/10.1088/2053-1591/aa846f>.
- [16] Q. Shao, P. Wang, X. Huang, Opportunities and challenges of interface engineering in bimetallic nanostructure for enhanced electrocatalysis, *Adv. Funct. Mater.* 29 (2019) 1806419, <https://doi.org/10.1002/adfm.201806419>.
- [17] Y. Xia, T. Yang, Z. Wang, T. Mao, Z. Hong, J. Han, D.L. Peng, G. Yue, Van der waals forces between S and P ions at the Co-P-C@MoS₂/C heterointerface with enhanced lithium/sodium storage, *Adv. Funct. Mater.* 202302830 (2023), <https://doi.org/10.1002/adfm.202302830>.
- [18] Z. Zhu, H. Huang, L. Liu, F. Chen, N. Tian, Y. Zhang, H. Yu, Chemically bonded α-Fe₂O₃/Bi₄MO₈Cl dot-on-plate Z-scheme junction with strong internal electric field for selective photo-oxidation of aromatic alcohols, *Angew. Chem. Int. Ed.* 61 (2022) e202203519, <https://doi.org/10.1002/anie.202203519>.
- [19] Z. Jiang, W. Zhou, C. Hu, X. Luo, W. Zeng, X. Gong, Y. Yang, T. Yu, W. Lei, C. Yuan, Interlayer-confined NiFe dual atoms within MoS₂ electrocatalyst for ultra-efficient acidic overall water splitting, *Adv. Mater.* 35 (2023) 2300505, <https://doi.org/10.1002/adma.202300505>.
- [20] F. Wang, S.S. Liu, Z. Feng, H. Fu, M. Wang, P. Wang, W. Liu, C.C. Wang, High-efficient peroxymonosulfate activation for rapid atrazine degradation by FeSx@MoS₂ derived from MIL-88A(Fe), *J. Hazard. Mater.* 440 (2022) 129723, <https://doi.org/10.1016/j.jhazmat.2022.129723>.
- [21] J. Qi, X. Yang, P.-Y. Pan, T. Huang, X. Yang, C.-C. Wang, W. Liu, Interface Engineering of Co(OH)₂ nanosheets growing on the KNbO₃ perovskite based on electronic structure modulation for enhanced peroxymonosulfate activation, *Environ. Sci. Technol.* 56 (2022) 5200–5212, <https://doi.org/10.1021/acs.est.1c08806>.
- [22] J. Hu, L. Yu, J. Deng, Y. Wang, K. Cheng, C. Ma, Q. Zhang, W. Wen, S. Yu, Y. Pan, J. Yang, H. Ma, F. Qi, Y. Wang, Y. Zheng, M. Chen, R. Huang, S. Zhang, Z. Zhao, J. Mao, X. Meng, Q. Ji, G. Hou, X. Han, X. Bao, Y. Wang, D. Deng, Sulfur vacancy-rich MoS₂ as a catalyst for the hydrogenation of CO₂ to methanol, *Nat. Catal.* 4 (2021) 242–250, <https://doi.org/10.1038/s41929-021-00584-3>.
- [23] M. Kim, M.A.R. Anjum, M. Choi, H.Y. Jeong, S.H. Choi, N. Park, J.S. Lee, Covalent OD–2D heterostructuring of Co₉S₈–MoS₂ for enhanced hydrogen evolution in all pH electrolytes, *Adv. Funct. Mater.* 30 (2020) 2002536, <https://doi.org/10.1002/adfm.202002536>.
- [24] Q. Yan, C. Lian, K. Huang, L. Liang, H. Yu, P. Yin, J. Zhang, M. Xing, Constructing an acidic microenvironment by MoS₂ in heterogeneous Fenton reaction for pollutant control, *Angew. Chem. Int. Ed.* 60 (2021) 17155–17163, <https://doi.org/10.1002/anie.202105736>.
- [25] Y. Liu, Y. Chen, Y. Tian, T. Sakthivel, H. Liu, S. Guo, H. Zeng, Z. Dai, Synergizing hydrogen spillover and deprotonation by the internal polarization field in a MoS₂/NiPS₃ vertical heterostructure for boosted water electrolysis, *Adv. Mater.* 34 (2022) 2203615, <https://doi.org/10.1002/adma.202203615>.
- [26] S. Li, X. Chen, M. Li, C. Xue, Y. Long, W. Liu, Z. Cao, X. Tong, W. Huang, D. Liu, Hollow Co₃S₄ polyhedron decorated with interlayer-expanded MoS₂ nanosheets for efficient tetracycline removal from aqueous solution, *Chem. Eng. J.* 441 (2022) 136006, <https://doi.org/10.1016/j.cej.2022.136006>.
- [27] L. Lyu, C. Lu, Y. Sun, W. Cao, T. Gao, C. Hu, Low consumption Fenton-like water purification through pollutants as electron donors substituting H₂O₂ consumption via twofold cation-π over MoS₂ cross-linking g-C₃N₄ hybrid, *Appl. Catal., B* 320 (2023) 121871, <https://doi.org/10.1016/j.apcatb.2022.121871>.
- [28] Z. Guo, X. Wang, Atomic layer deposition of the metal pyrites FeS₂, CoS₂, and NiS₂, *Angew. Chem. Int. Ed.* 57 (2018) 5898–5902, <https://doi.org/10.1002/anie.201803092>.
- [29] H. Gao, T. Zhou, Y. Zheng, Q. Zhang, Y. Liu, J. Chen, H. Liu, Z. Guo, CoS quantum dot nanoclusters for high-energy potassium-ion batteries, *Adv. Funct. Mater.* 27 (2017) 1702634, <https://doi.org/10.1002/adfm.201702634>.
- [30] Q. Zhang, D. Xu, A. Cai, X. Hu, X. Li, W. Peng, Y. Li, F. Zhang, X. Fan, Chemoselective hydrogenation of nitro compounds by MoS₂ via introduction of independent active hydrogen-donating sites, *ACS Catal.* 12 (2022) 12170–12178, <https://doi.org/10.1021/acscatal.2c03130>.
- [31] J.L. Verble, T.J. Wieting, Lattice mode degeneracy in MoS₂ and other layer compounds, *Phys. Rev. Lett.* 25 (1970) 362–365, <https://doi.org/10.1103/PhysRevLett.25.362>.
- [32] D. Kong, H. Wang, J.J. Cha, M. Pasta, K.J. Koski, J. Yao, Y. Cui, Synthesis of MoS₂ and MoSe₂ films with vertically aligned layers, *Nano Lett.* 13 (2013) 1341–1347, <https://doi.org/10.1021/nl400258t>.
- [33] Y.-H. Chang, C.-T. Lin, T.-Y. Chen, C.-L. Hsu, Y.-H. Lee, W. Zhang, K.-H. Wei, L.-J. Li, Highly efficient electrocatalytic hydrogen production by MoS_x grown on graphene-protected 3D Ni foams, *Adv. Mater.* 25 (2013) 756–760, <https://doi.org/10.1002/adma.201202920>.
- [34] Z. Fang, Y. Liu, J. Qi, Z.-F. Xu, T. Qi, L. Wang, Establishing a high-speed electron transfer channel via CuS/MIL-Fe heterojunction catalyst for photo-Fenton degradation of acetaminophen, *Appl. Catal., B* 320 (2023) 121979, <https://doi.org/10.1016/j.apcatb.2022.121979>.
- [35] Y. Yao, Y. Wang, T. Lu, J. Zhang, K. Hu, H. Zhang, T. Pukala, Y. Liu, X. Duan, S. Wang, In-plane implanting carbon rings into carbon nitride to intriguing nonradical photodegradation, *Appl. Catal., B* 342 (2024) 123363, <https://doi.org/10.1016/j.apcatb.2023.123363>.
- [36] F. He, Y. Lu, G. Jiang, Y. Zhang, P. Dong, X. Liu, Y. Wang, C. Zhao, S. Wang, X. Duan, J. Zhang, S. Wang, Unveiling the dual charge modulation of built-in electric field in metal-free photocatalysts for efficient photo-Fenton-like reaction, *Appl. Catal., B* 341 (2024) 123307, <https://doi.org/10.1016/j.apcatb.2023.123307>.
- [37] Y. Zhou, Y. Yao, R. Zhao, X. Wang, Z. Fu, D. Wang, H. Wang, L. Zhao, W. Ni, Z. Yang, Y.M. Yan, Stabilization of Cu⁺ via strong electronic interaction for selective and stable CO₂ electroreduction, *Angew. Chem. Int. Ed.* 61 (2022) e202205832, <https://doi.org/10.1002/anie.202205832>.
- [38] Y. Chen, G. Zhang, H. Liu, J. Qu, Confining free radicals in close vicinity to contaminants enables ultrafast Fenton-like processes in the interspacing of MoS₂ membranes, *Angew. Chem. Int. Ed.* 58 (2019) 8134–8138, <https://doi.org/10.1002/anie.201903531>.

[39] S. Wang, Y. Liu, J. Wang, Peroxymonosulfate activation by Fe-Co-O-codoped graphite carbon nitride for degradation of sulfamethoxazole, Environ. Sci. Technol. 54 (2020) 10361–10369, <https://doi.org/10.1021/acs.est.0c03256>.

[40] T. Liu, S. Xiao, N. Li, J. Chen, X. Zhou, Y. Qian, C.H. Huang, Y. Zhang, Water decontamination via nonradical process by nanoconfined Fenton-like catalysts, Nat. Commun. 14 (2023) 2881, <https://doi.org/10.1038/s41467-023-38677-1>.

[41] Z. Yang, J. Qian, A. Yu, B. Pan, Singlet oxygen mediated iron-based Fenton-like catalysis under nanoconfinement, Proc. Natl. Acad. Sci. 116 (2019) 6659–6664, <https://doi.org/10.1073/pnas.1819382116>.

[42] S. Zhang, H. Gao, X. Xu, R. Cao, H. Yang, X. Xu, J. Li, MOF-derived CoN/N-C@SiO₂ yolk-shell nanoreactor with dual active sites for highly efficient catalytic advanced oxidation processes, Chem. Eng. J. 381 (2020) 122670, <https://doi.org/10.1016/j.cej.2019.122670>.

[43] L. Hou, X. Li, Q. Yang, F. Chen, S. Wang, Y. Ma, Y. Wu, X. Zhu, X. Huang, D. Wang, Heterogeneous activation of peroxymonosulfate using Mn-Fe layered double hydroxide: Performance and mechanism for organic pollutant degradation, Sci. Total. Environ. 663 (2019) 453–464, <https://doi.org/10.1016/j.scitotenv.2019.01.190>.

[44] C. Qi, X. Liu, Y. Li, C. Lin, J. Ma, X. Li, H. Zhang, Enhanced degradation of organic contaminants in water by peroxydisulfate coupled with bisulfite, J. Hazard. Mater. 328 (2017) 98–107, <https://doi.org/10.1016/j.jhazmat.2017.01.010>.

[45] L. Peng, Y. Shang, B. Gao, X. Xu, Co₃O₄ anchored in N, S heteroatom co-doped porous carbons for degradation of organic contaminant: role of pyridinic N-Co binding and high tolerance of chloride, Appl. Catal., B 282 (2021) 119484, <https://doi.org/10.1016/j.apcatb.2020.119484>.

[46] B. Li, C. Li, R. Qu, N. Wu, Y. Qi, C. Sun, D. Zhou, Z. Wang, Effects of common inorganic anions on the ozonation of polychlorinated diphenyl sulfides on silica gel: Kinetics, mechanisms, and theoretical calculations, Water Res 186 (2020), <https://doi.org/10.1016/j.watres.2020.116358>.

[47] F. Li, Z. Lu, T. Li, P. Zhang, C. Hu, Origin of the excellent activity and selectivity of a single-atom copper catalyst with unsaturated Cu-N₂ sites via peroxydisulfate activation: Cu(III) as a dominant oxidizing species, Environ. Sci. Technol. 56 (2022) 8765–8775, <https://doi.org/10.1021/acs.est.2c00369>.

[48] H. Daims, E.V. Lebedeva, P. Pjevac, P. Han, C. Herbold, M. Albertsen, N. Jehmlich, M. Palatinzky, J. Vierheilig, A. Bulaev, R.H. Kirkegaard, M. von Bergen, T. Rattei, B. Bender, P.H. Nielsen, M. Wagner, Complete nitrification by Nitrospira bacteria, Nature 528 (2015) 504–509, <https://doi.org/10.1038/nature16461>.

[49] Z. Fang, J. Qi, W. Chen, L. Zhang, J. Wang, C. Tian, Q. Dai, W. Liu, L. Wang, Defect engineering-mediated Co₉S₈ with unexpected catalytic selectivity for heterogeneous Fenton-like reaction: Unveiling the generation route of ¹O₂ in V_s active site, Appl. Catal., B 338 (2023) 123084, <https://doi.org/10.1016/j.apcatb.2023.123084>.

[50] R. Zhang, Y. Yang, C.-H. Huang, L. Zhao, P. Sun, Kinetics and modeling of sulfonamide antibiotic degradation in wastewater and human urine by UV/H₂O₂ and UV/PDS, Water Res 103 (2016) 283–292, <https://doi.org/10.1016/j.watres.2016.07.037>.

[51] X. Nie, G. Li, S. Li, Y. Luo, W. Luo, Q. Wan, T. An, Highly efficient adsorption and catalytic degradation of ciprofloxacin by a novel heterogeneous Fenton catalyst of hexapod-like pyrite nanosheets mineral clusters, Appl. Catal., B 300 (2022) 120734, <https://doi.org/10.1016/j.apcatb.2021.120734>.

[52] Z. Wang, E. Almatrafi, H. Wang, H. Qin, W. Wang, L. Du, S. Chen, G. Zeng, P. Xu, Cobalt single atoms anchored on oxygen-doped tubular carbon nitride for efficient peroxymonosulfate activation: simultaneous coordination structure and morphology modulation, Angew. Chem. Int. Ed. 61 (2022) e202202338, <https://doi.org/10.1002/anie.202202338>.

[53] N. Li, R. Li, X. Duan, B. Yan, W. Liu, Z. Cheng, G. Chen, L. Hou, S. Wang, Correlation of active sites to generated reactive species and degradation routes of organics in peroxymonosulfate activation by Co-loaded carbon, Environ. Sci. Technol. 55 (2021) 16163–16174, <https://doi.org/10.1021/acs.est.1c06244>.

[54] N. Zheng, X. Tang, Y. Lian, Z. Ou, Q. Zhou, R. Wang, Z. Hu, Low-valent copper on molybdenum triggers molecular oxygen activation to selectively generate singlet oxygen for advanced oxidation processes, J. Hazard. Mater. 452 (2023) 131210, <https://doi.org/10.1016/j.jhazmat.2023.131210>.

[55] S. Zuo, Y. Ding, L. Wu, F. Yang, Z. Guan, S. Ding, D. Xia, X. Li, D. Li, Revealing the synergistic mechanism of the generation, migration and nearby utilization of reactive oxygen species in FeOCl-MOF yolk-shell reactors, Water Res 231 (2023) 119631, <https://doi.org/10.1016/j.watres.2023.119631>.

[56] P. Zhang, Y. Yang, X. Duan, Y. Liu, S. Wang, Density functional theory calculations for insight into the heterocatalyst reactivity and mechanism in persulfate-based advanced oxidation reactions, ACS Catal. 11 (2021) 11129–11159, <https://doi.org/10.1021/acscatal.1c03099>.

[57] X.L. Wu, S. Liu, Y. Li, M. Yan, H. Lin, J. Chen, S. Liu, S. Wang, X. Duan, Directional and ultrafast charge transfer in oxygen-vacancy-rich ZnO@single-atom cobalt core-shell junction for photo-Fenton-like reaction, Angew. Chem. Int. Ed. 62 (2023) e202305639, <https://doi.org/10.1002/anie.202305639>.

[58] J. Liang, L. Fu, K. Gao, X. Duan, Accelerating radical generation from peroxymonosulfate by confined variable Co species toward ciprofloxacin mineralization: ROS quantification and mechanisms elucidation, Appl. Catal., B 315 (2022) 121542, <https://doi.org/10.1016/j.apcatb.2022.121542>.

[59] M. Li, S. You, X. Duan, Y. Liu, Selective formation of reactive oxygen species in peroxymonosulfate activation by metal-organic framework-derived membranes: A defect engineering-dependent study, Appl. Catal., B 312 (2022) 121419, <https://doi.org/10.1016/j.apcatb.2022.121419>.

[60] X. Yang, J. Duan, J. Qi, X. Li, J. Gao, Y. Liang, S. Li, T. Duan, W. Liu, Modulating the electron structure of Co-3d in Co₃O_{4-x}/WO_{3.72} for boosting peroxymonosulfate activation and degradation of sulfamerazine: Roles of high-valence W and rich oxygen vacancies, J. Hazard. Mater. 445 (2023) 130576, <https://doi.org/10.1016/j.jhazmat.2022.130576>.

[61] M. Gu, L. Jiang, S. Zhao, H. Wang, M. Lin, X. Deng, X. Huang, A. Gao, X. Liu, P. Sun, X. Zhang, Deciphering the space charge effect of the p-n junction between copper sulfides and molybdenum selenides for efficient water electrolysis in a wide pH range, ACS Nano 16 (2022) 15425–15439, <https://doi.org/10.1021/acsnano.2c07255>.

[62] W. Gao, X. Zhao, T. Zhang, X. Yu, Y. Ma, E.C. dos Santos, J. White, H. Liu, Y. Sang, Construction of diluted magnetic semiconductor to endow nonmagnetic semiconductor with spin-regulated photocatalytic performance, Nano Energy 110 (2023), <https://doi.org/10.1016/j.nanoen.2023.108381>.

[63] H. Khan, S.A. Shah, Wu Rehman, F. Chen, CoS₂ nanoparticles-decorated MoS₂/rGO nanosheets as an efficient electrocatalyst for ultrafast hydrogen evolution, Adv. Mater. Interfaces 9 (2021) 2101294, <https://doi.org/10.1002/admi.202101294>.

[64] S. Hariganeesh, S. Vadivel, D. Maruthamani, M. Kumaravel, A. Habibi-Yangieh, Facile solvothermal synthesis of Novel CuCo₂S₄/g-C₃N₄ nanocomposites for visible-Light photocatalytic applications, J. Inorg. Organomet. Polym. Mater. 28 (2018) 1276–1285, <https://doi.org/10.1007/s10904-018-0828-5>.

[65] X. Liu, S. Lu, Y. Liu, W. Meng, B. Zheng, Adsorption of sulfamethoxazole (SMZ) and ciprofloxacin (CIP) by humic acid (HA): characteristics and mechanism, RSC Adv. 7 (2017) 50449–50458, <https://doi.org/10.1039/c7ra06231a>.

[66] F. Wang, H. Fu, F.X. Wang, X.W. Zhang, P. Wang, C. Zhao, C.C. Wang, Enhanced catalytic sulfamethoxazole degradation via peroxymonosulfate activation over amorphous Co₅x@SiO₂ nanocages derived from ZIF-67, J. Hazard. Mater. 423 (2022) 126998, <https://doi.org/10.1016/j.jhazmat.2021.126998>.

[67] X. Wang, Z. Xiong, H. Shi, Z. Wu, B. Huang, H. Zhang, P. Zhou, Z. Pan, W. Liu, B. Lai, Switching the reaction mechanisms and pollutant degradation routes through active center size-dependent Fenton-like catalysis, Appl. Catal. B 329 (2023) 122569, <https://doi.org/10.1016/j.apcatb.2023.122569>.

[68] C. Chen, L. Liu, Y. Li, W. Li, L. Zhou, Y. Lan, Y. Li, Insight into heterogeneous catalytic degradation of sulfamethazine by peroxymonosulfate activated with CuCo₂O₄ derived from bimetallic oxalate, Chem. Eng. J. 384 (2020) 123257, <https://doi.org/10.1016/j.cej.2019.123257>.

[69] Y. Li, H. Dong, L. Li, J. Xiao, S. Xiao, Z. Jin, Efficient degradation of sulfamethazine via activation of percarbonate by chalcocite, Water Res 202 (2021) 117451, <https://doi.org/10.1016/j.watres.2021.117451>.

[70] Y. Wu, J. Chen, H. Che, X. Gao, Y. Ao, P. Wang, Boosting 2e⁻ oxygen reduction reaction in garland carbon nitride with carbon defects for high-efficient photocatalysis-self-Fenton degradation of 2,4-dichlorophenol, Appl. Catal., B 307 (2022) 121185, <https://doi.org/10.1016/j.apcatb.2022.121185>.